JAMES | Journal of Advances in Modeling Earth Systems

RESEARCH ARTICLE
10.1029/2022MS003056

Key Points:

- The $z^{\sim}$ time-filtered vertical coordinate is tested in a global 1/4° forced Nucleus for European Modeling of the Ocean configuration
- We confirm that $z^{\sim}$ converts Eulerian vertical velocities on time scales of a few days into coordinate displacements
- $z^{\sim}$ tends to reduce temperature and salinity biases, particularly at thermocline depths, without adverse effects on other metrics

Correspondence to:

A. Megann,
apm@noc.ac.uk

Citation:

Megann, A., Chanut, J., & Storkey, D. (2022). Assessment of the $z^{\sim}$ time-filtered Arbitrary Lagrangian-Eulerian coordinate in a global eddy-permitting ocean model. *Journal of Advances in Modeling Earth Systems*, *14*, e2022MS003056. https://doi.org/10.1029/2022MS003056

Received 11 MAR 2022
Accepted 13 OCT 2022

Author Contributions:

Conceptualization: Alex Megann
Data curation: David Storkey
Formal analysis: Alex Megann
Funding acquisition: Alex Megann
Investigation: Alex Megann
Methodology: Alex Megann, Jérôme Chanut, David Storkey
Project Administration: Alex Megann
Software: Alex Megann, Jérôme Chanut
Validation: Alex Megann
Visualization: Alex Megann
Writing – original draft: Alex Megann
Writing – review & editing: Alex Megann, Jérôme Chanut, David Storkey

Assessment of the $z^{\sim}$ Time-Filtered Arbitrary Lagrangian-Eulerian Coordinate in a Global Eddy-Permitting Ocean Model

Alex Megann[1], Jérôme Chanut[2], and David Storkey[3]

[1]National Oceanography Centre, Southampton, UK, [2]Mercator Ocean International, Toulouse, France, [3]Met Office, Exeter, UK

Abstract A recognized deficiency of ocean models with a constant-depth vertical coordinate is for truncation errors in the vertical advection scheme to result in spurious numerical mixing of tracers, which can be substantially stronger than that prescribed by the model's mixing scheme. The $z^{\sim}$ vertical coordinate allows vertical levels to displace in a Lagrangian fashion on time scales shorter than a few days, but reverts to fixed levels on longer timescales, and is intended to reduce numerical mixing from transient vertical motions such as internal waves and tides. An assessment of $z^{\sim}$ in a 1/4° global implementation of the Nucleus for European Modeling of the Ocean model is presented. It is shown that, in the presence of near-inertial gravity waves in the North Atlantic, $z^{\sim}$ significantly reduces Eulerian vertical velocities with respect to those in a simulation with the default z^{*} vertical coordinate; that the vertical coordinate approaches an isopycnal, or adiabatic, surface on short timescales; and that both tendencies are enhanced when the $z^{\sim}$ timescale parameters are lengthened with respect to the default settings. Analysis based on density transformation rates shows that numerical mixing is consistently reduced by of order 10% as the $z^{\sim}$ timescales are lengthened. The realism of the model simulation with different timescale parameters is assessed in the global domain, and it is shown that drifts in temperature and salinity, and the spindown in z^{*} of the Antarctic Circumpolar Current, are reduced with $z^{\sim}$, without incurring significant drawbacks in other metrics such as the strength of the overturning circulation or sea ice cover.

Plain Language Summary In ocean models where the vertical coordinate is located at fixed depth levels, spurious, or non-physical, vertical numerical mixing of the temperature and salinity fields is known to occur. A significant part of this is caused by "truncation errors" in the model code that cause spurious mixing when vertical motions in internal waves in the ocean repeatedly carry water parcels back and forth between the layers of the model. We investigate the $z^{\sim}$ vertical coordinate, which moves vertically with internal wave motions on timescales shorter than a few days, but tends to fixed levels at long timescales, in an ensemble of integrations of a global Nucleus for European Modeling of the Ocean model. We show that a measure of total mixing (the effective diffusivity) derived from the rate of change of density in the ocean interior is reduced with $z^{\sim}$ of order 10%. Furthermore, we show that $z^{\sim}$ consistently reduces biases in the temperature and salinity fields, particularly in the depth range 300–500 m, and also reduces the unrealistic spin-down of the Antarctic Circumpolar Current, without significant adverse effects on other aspects of the model performance.

1. Introduction

We may define numerical mixing in ocean models as mixing that does not arise from the explicit mixing scheme of the model. This extra spurious mixing may be as large as, or even substantially larger than, the explicit mixing in a given model (e.g., A. Megann, 2018), and has the potential to bias the representation of heat uptake by the ocean from the atmosphere in coupled climate models, as well as causing unrealistic drifts in internal temperature and salinity fields. Much of the numerical mixing is caused by truncation errors in the tracer advection scheme (Griffies et al., 2000), and manifests in several distinct ways, their relative severity depending on the model grid and the choice of numerical scheme. One manifestation is in the representation of deep overflows, such as those over the sills between the North Atlantic and the Arctic Ocean, and this is typically poor in models with a constant-depth vertical coordinate (Colombo et al., 2020; Dickson et al., 2008; Ilıcak, 2016; Winton et al., 1998). In this case, the spuriously high rate of entrainment of the overflow waters results in unrealistically warm and thick bottom waters downstream of the sills. This may be remedied by the use of terrain-following coordinates (e.g.,

Shchepetkin, 2015) or of isopycnic coordinates (A. P. Megann et al., 2010; Bleck & Smith, 1990). Another contribution is from numerical noise in the velocity field in regions where the mesoscale is poorly resolved, which tends to cause numerical instability in flow regimes with large cell Reynolds number (e.g., Bryan et al., 1975; Griffies & Hallberg, 2000; Ilıcak et al., 2012); this is a particular problem for global grids with "eddy-permitting" resolution of around 1/4°, in which a large portion of the grid does not resolve the first Rossby radius (Hallberg, 2013). A. Megann and Storkey (2021, henceforth referred to as MS2021) demonstrated that increasing the biharmonic viscosity from the default value in a 1/4° global Nucleus for European Modeling of the Ocean (NEMO) model configuration consistently led to reductions in numerical mixing and in large-scale temperature drifts, without adverse effects on most other metrics of model realism. Additional contributions to numerical mixing may arise from projection of truncation errors in horizontal tracer advection into the dianeutral direction (Griffies et al., 2000), and from non-alignment of the nominally iso-neutral explicit diffusion with the local neutral surface (Griffies et al., 1998), which particularly manifests in regimes where there is a significant mean isopycnal slope.

A third contribution to numerical mixing arises from net vertical advection of tracers across coordinate surfaces by relatively high-frequency processes such as internal waves and tides, and this is likely to be the dominant contribution in regimes where the isopycnals are relatively flat. Near-inertial gravity waves (NIGWs; Alford et al., 2016) and internal tides (Wunsch, 1975) are typically characterized by periods of between 12 and 30 hr in nature, and their associated vertical velocities may reach several tens of meters per day. Such waves have the potential to contribute a significant fraction to the global ocean mixing budget when they break (Gargett & Holloway, 1984), but in general they propagate nearly adiabatically (i.e., without much mixing). In numerical models, by contrast, truncation errors in the advection scheme tend to add an irreversible, or diffusive, component to tracer advection, and these transient vertical velocities add a spurious component to the vertical (or diapycnal) mixing (Griffies et al., 2000; Leclair & Madec, 2011). While this contribution to numerical mixing is an intrinsic property of fixed-coordinate models, pure isopycnic models, such as the Miami Isopycnic-Coordinate Model (MICOM; Bleck & Smith, 1990) and the Generalized Ocean Layered Dynamics model (GOLD; Hallberg & Adcroft, 2009), which use a potential density coordinate in the vertical, do not exhibit numerical mixing from this source, since vertical advection of tracers across coordinate surfaces is by construction zero in this model formalism. Such models, nevertheless, have disadvantages such as the challenge of finding a vertical density coordinate that is everywhere monotonic in the vertical, and problems with detrainment from a mixed layer with variable density into interior layers with specified densities.

In the last two decades, considerable effort has been put into developing models which combine the advantages of depth-coordinate and isopycnic models by using constant-depth levels in the upper ocean and isopycnic coordinates at depth; these include the Hybrid-Coordinate Ocean Model (HYCOM; Bleck, 2002) and version six of the Modular Ocean Model (MOM6; Adcroft et al., 2019). Controlled studies, in which a coupled model has a depth-coordinate ocean component replaced with an isopycnal model of the same resolution, have demonstrated that this type of model has reduced levels of numerical mixing from all three of the mechanisms mentioned above, when compared with comparable depth-coordinate models (A. P. Megann et al., 2010; Dunne et al., 2012), as evidenced by colder bottom temperatures, a sharper thermocline, and slower drifts in temperature and salinity fields, although Adcroft et al. (2019) report that issues still remain with the Denmark Strait overflow in MOM6 even when used with a hybrid vertical coordinate. Generalized Arbitrary Lagrangian-Eulerian frameworks (Adcroft & Hallberg, 2006; Griffies et al., 2020) provide a generalized approach to choosing the vertical coordinate most appropriate for each regime of the ocean: fixed-depth (either geopotential or terrain-following), where the divergence of lateral flow results in vertical velocities across the coordinate surfaces; quasi-Lagrangian, where the coordinate surface is displaced vertically according to the divergence of the flow; or some intermediate combination. This framework has the potential to approach an optimum configuration in terms of reducing numerical mixing from tracer advection across coordinate surfaces, although in practice it may not be obvious what metrics might determine such an optimum.

The default vertical coordinate in version four of the NEMO v4 model (Madec et al., 2019) is the nonlinear free surface, or Variable Volume Layer, scheme (Adcroft & Campin, 2004; Levier et al., 2007; Stacey et al., 1995), usually referred to in shorthand as z^*. This represents external gravity waves as changes to the layer vertical scale e_3 at each level scaled with the surface height anomaly over the water column. It allows the ocean volume to change as a result of mass fluxes through the surface, and so conserves tracers exactly, in contrast to the older linear free surface, provided that some modifications to the leap-frog time stepping are implemented (Leclair & Madec, 2009). This coordinate system can be summarized as follows: barotropic vertical motion is

quasi-Lagrangian, in the sense that the external mode does not cause advection across the coordinate surfaces, while baroclinic vertical motion is quasi-Eulerian, involving material advection across the coordinate interfaces, and it is the latter that contributes to numerical mixing. The $z^{\sim}$ coordinate (Leclair & Madec, 2011, hereafter referred to as LM2011) is a modification to the z^* vertical coordinate in NEMO in which the external mode, and internal motions at low frequencies, are treated within a Eulerian framework as in z^*, while internal vertical motions at high frequencies are represented as Lagrangian. To clarify, at low frequencies internal vertical motions manifest as Eulerian vertical velocities crossing the coordinate surface, while at high frequencies the coordinate surface itself is displaced, consistent with the divergence of the horizontal flow. The frequency division is accomplished by a first-order exponential filter, with a timescale $\tau_{\sim}$ of a few days, while the $z^{\sim}$ coordinate itself is restored to z^* with a second timescale τ_z of a few weeks. LM2011 demonstrated the effectiveness of $z^{\sim}$ in an idealized channel domain in suppressing by a factor of five the numerical mixing from forced internal waves, although until the present study it has not been comprehensively tested in NEMO in a global domain. We note in passing a strong correspondence between $z^{\sim}$ and the "slack" process in HYCOM (Bleck, 2002), where high-frequency internal waves in the near-surface geopotential layers of the hybrid grid are treated in a similar Lagrangian way to reduce numerical mixing.

Several approaches have been used to quantify the sensitivity of numerical mixing to the vertical coordinate in idealized domains. Ilıcak et al. (2012) and Ilıcak (2016) used the Reference Potential Energy (RPE) method to analyze numerical mixing in a suite of model configurations in idealized domains, including lock exchange and a periodic channel: in the three models with fixed vertical coordinates, most of the numerical mixing was attributed to truncation errors in the advection scheme, with a relatively small contribution from cabbeling. In the pure isopycnic model (GOLD), by contrast, the only source of numerical mixing was the latter process. Petersen et al. (2015) used the Model for Prediction Across Scales-Ocean (MPAS-Ocean) model as a platform to evaluate the choice of vertical coordinate on numerical mixing in some idealized test cases, comparing the unstructured-grid MPAS with the orthogonal-grid POP and MOM ocean models in z^*, $z^{\sim}$ with a 5-day time scale $\tau_{\sim}$, terrain-following and pure isopycnic coordinate configurations, as well as in a global domain at several resolutions between 15 and 120 km. They used a similar potential energy metric to that employed in the studies by Ilıcak et al. to diagnose the total mixing, concluding that MPAS-Ocean exhibited substantially lower numerical mixing than did POP or MOM, attributing the improvement partly to reduced truncation errors arising from the hexagonal grid used by their model, and partly to the implementation of the flux-corrected tracer transport (FCT) scheme on the MPAS-Ocean grid. Gibson et al. (2017) applied the RPE approach to lock exchange simulations based on the MPAS-Ocean, MITgcm, MOM5 and MOM6 models, and separated the contributions of horizontal and vertical tracer advection to spurious mixing. They found that increasing horizontal resolution reduced the numerical mixing from horizontal advection, but this was not strongly sensitive to the choice of advection scheme; instead, reducing grid-scale vertical velocity noise had a stronger effect, consistent with the results of Ilıcak et al. (2012) and of MS2021. The numerical mixing was found to be much more strongly sensitive to the choice of vertical coordinate: the $z^{\sim}$ cases showed reductions in spurious mixing from both horizontal and vertical advection, that from the former being attributed to the coordinate surface on short timescales being more closely aligned with isopycnal surfaces.

Holmes et al. (2021) evaluated an internal heat budget in individual water columns during runtime in a suite of simulations using the MOM5 depth-coordinate ocean model and the CICE sea ice model at 1/4° and 1/10° horizontal resolution and several choices of vertical resolutions, as well as a range of parameter settings for vertical and isoneutral diffusion schemes. From the heat budget, they derived an estimate of numerical mixing in temperature classes, and concluded that the numerical contribution to the diathermal heat transport was of comparable magnitude to that associated with explicit parameterizations. Numerical mixing was found to be particularly prominent in the tropical thermocline, where it was sensitive to the vertical diffusivity and resolution, and they ascribed this to a combination of large vertical and horizontal temperature gradients and noise in the velocity field at the grid scale, particularly in its horizontal components.

Lee et al. (2002), Urakawa and Hasumi (2014), and A. Megann (2018) used the density transformation framework of Walin (1982) to derive a zonal mean effective diapycnal diffusivity in domains with realistic boundaries and forcing, which was compared with the explicit diffusivity derived from the subgrid mixing scheme. This approach has the advantage, relative to the potential energy approaches mentioned above, of allowing analysis of a fully forced, and hence more realistic, model configuration, more similar to the situation in a climate model than in the spin-down and spin-up simulations of the former studies. A. Megann (2018) applied this technique

to an eddy-permitting global NEMO configuration, finding that the rate of density transformation in the model was in some regions several times larger than that prescribed by the explicit mixing alone, and that the effective diffusivity was between 5 and 10 larger than the explicit diffusivity in density classes typical of intermediate and deep waters, and in the tropics and mid-latitudes. This study associated the numerical mixing with transient vertical velocities of up to two orders of magnitude larger than the mean large-scale upwelling and downwelling velocities, characterizing these vertical motions as having a horizontal length scale close to the grid scale, but as being coherent over more than 1,000 m in the vertical.

In this paper we use an ensemble of global 1/4° forced NEMO integrations to investigate the effectiveness of the $z^{\sim}$ vertical coordinate in a realistic ocean domain. We use local, one-dimensional metrics to compare the performance of $z^{\sim}$ in a region of the North Atlantic where NIGWs have large amplitudes, and to quantify the sensitivity of $z^{\sim}$ to its two timescale parameters. We then evaluate global metrics, including the effective diapycnal diffusivity κ_{eff}, global water mass drifts and biases, large-scale circulation indices and ice cover, to confirm that $z^{\sim}$ robustly reduces numerical mixing, and that it thereby has an overall positive effect on the realism of the model. The model code base and configuration are closely related to those used by MS2021, and we shall explicitly compare the effects of $z^{\sim}$ on large scale metrics with those of increasing the viscosity in a configuration with the z^* coordinate, as described in the latter paper.

In Section 2, we describe the model and the experimental design, and Section 3 is an overview of the analysis used in the paper. In Section 4, we use NIGWs in the North Atlantic as a testbed to verify the functioning of the $z^{\sim}$ coordinate in this configuration. In Section 5, we present analysis of the sensitivity of the global fields and large-scale circulation of the model to the vertical coordinate, and Section 6 is a summary and discussion.

2. Model Description and Experimental Design

2.1. Model Description

The GO8p0.1 model configuration is based on the GO6/GO7 ocean configurations (Storkey et al., 2018), the former being the ocean component of the GC3.1 coupled model (Williams et al., 2018) and the UK Earth System Model (Sellar et al., 2019), the latter two models forming the UK's contribution to CMIP6. It has, as far as is feasible, the same physics and parameterizations as GO6/GO7, with two major exceptions. The first is that the code base for the ocean component is upgraded from version 3.6-stable to version 4.0.1 of the Nucleus for European Marine Modeling (Madec et al., 2019) ocean model. The second is that the sea ice model is changed from CICE to the new Sea Ice modeling Integrated Initiative model (SI^3), which is based on version three of the Louvain-le-Neuve Ice Model (Rousset et al., 2015), and is now an integral part of the NEMO v4 code.

The model is otherwise identical to that in GO6/GO7; the latter configuration is described in detail in Storkey et al. (2018), but we summarize the main features here. The grid is the eORCA025 extended global 1/4° resolution grid (Barnier et al., 2006), with a quasi-isotropic bipolar grid with poles at land points in Siberia and Canada, a southern extension to allow simulation of the Antarctic ice shelves, and a Mercator projection grid elsewhere. We emphasize that, apart from the change in sea ice model, the physics and parameter choices are almost identical between the control simulation described by MS2021 and the z^* control in the present ensemble.

The default viscosity scheme is a bilaplacian viscosity which has a reference value of -1.5×10^{11} m^4s^{-1} at the equator, with values reduced polewards as the cube of the maximum grid cell dimension in order to avoid instability in the momentum diffusion equation (see Griffies & Hallberg, 2000). Although MS2001 demonstrated that this choice of viscosity is lower than optimal, resulting in cell Reynolds numbers larger than the critical value over a significant portion of the model domain and hence higher numerical mixing, we maintain the default viscosity value to preserve traceability to earlier configurations. The horizontal pressure gradient scheme follows a standard density Jacobian formulation (Shchepetkin & McWilliams, 2003).

Tracer advection is performed by second-order FCT scheme, also known as total variation diminishing (TVD; Zalesak, 1979), for both horizontal and vertical advection of tracers. We note that this is essentially the same scheme as used in the "TVD" experiments described by LM2011. Lateral diffusion of tracers is along isoneutral surfaces, with a coefficient of 150 m^2s^{-1}; the default in NEMO v4 is the scheme of Redi (1982), as implemented by Cox (1987). No mesoscale eddy parameterization scheme is used. The vertical mixing scheme is a modified version of the Turbulent Kinetic Energy scheme (Gaspar et al., 1990; Madec et al., 2019), with a background

Table 1
Summary of Model Experiments

Experiment	Vertical coordinate	$\tau_{\sim}$ (days)	τ_z (days)
zstar	z^*	N/A	N/A
ztilde_5_30	$z^{\sim}$	5	30
ztilde_10_30	$z^{\sim}$	10	30
ztilde_20_30	$z^{\sim}$	20	30
ztilde_20_60	$z^{\sim}$	20	60
ztilde_40_60	$z^{\sim}$	40	60

Note. The two numbers in the experiment name refer respectively to the $z^{\sim}$ cutoff time parameter, $\tau_{\sim}$, and to the restoration time to z^*, τ_z.

vertical eddy diffusivity of 1.2×10^{-5} m^2s^{-1}, which decreases linearly with latitude from 15°N to 15°S toward the Equator. The current GO8 configuration has the tidal mixing parameterization of Simmons et al. (2004), which was applied in GO6, but since it is not present in the standard NEMO v4 release, is added to GO6 as a development branch (see Appendix B for details of the model sources).

The ocean is initialized at rest from a 1995–2004 average of the EN4 climatology (Good et al., 2013). The initial state of the sea ice is derived from a "bootstrap" initialization option in SI[3] which assigns sea ice wherever the initial SST is at the freezing point, with concentration 0.90 and thickness set to 3.0 m in the northern hemisphere and 1.0 m in the southern hemisphere. Surface forcing is with CORE2 interannual fields (Large & Yeager, 2009), with the following forcing frequencies: 6-hourly wind speed, air temperature and humidity; daily longwave and shortwave radiation, with a diurnal cycle applied to the latter; and monthly mean precipitation. This forcing is identical to that used in the experiments described by A. Megann (2018), Storkey et al. (2018), and A. Megann and Storkey (2021). The experiments are integrated from 1976 to 2005, with the last 10 years used for much of the analysis.

2.2. The $z^{\sim}$ Vertical Coordinate

The $z^{\sim}$ coordinate is summarized in Appendix A1. The configuration used here applies a set of modifications (described in Appendix A2) to the existing model code in NEMO v4.0 relating to the $z^{\sim}$ coordinate: selecting $z^{\sim}$ with the standard releases of either version 3.6-stable or NEMO v4 in a domain with realistic topography is found to lead to rapid and terminal instabilities in the model.

In the NEMO namelist an option is provided which ramps $z^{\sim}$ down to zero at the equator to increase numerical stability, but it was found in the present implementation that the model was stable with $z^{\sim}$ applied over the whole global grid, so this latter choice was used in all experiments.

2.3. Experimental Strategy

An ensemble of experiments was integrated to determine the effect of changing from z^* to $z^{\sim}$, and also the sensitivity to the time filtering applied for the latter coordinate, as follows:

1. $z^{\sim}$ compared with z^*;
2. $z^{\sim}$ cutoff time $\tau_{\sim}$ extended from the default of 5 days up to 40 days;
3. $z^{\sim}$ restoration time τ_z extended from the default of 30 days up to 60 days.

The experiments are listed in Table 1. With a timestep of 15 min, and running on 346 cores of the joint supercomputing system at the Met Office (MONSooN), the *zstar* experiment completed a year of integration in between 15 and 16 hr, corresponding to a throughput of around 5,400 CPU hours per model year. $z^{\sim}$ was found to be stable with the same timestep as used with z^*, in contrast with the experience of Gibson et al. (2017), where stability issues in their implementation of MPAS-Ocean forced a timestep of half that in their z^* configuration to be used. Nevertheless, $z^{\sim}$ in NEMO was found to incur a performance penalty in this configuration of between 15% and 18% in runtime relative to z^*, which comes mainly from solving additional 3-D advection with flux limiting and a diffusion term for internal thicknesses, and to a lesser extent from the computation of time filtered fluxes.

3. Analysis

3.1. Coordinate Displacement in Internal Waves

The main objectives of the $z^{\sim}$ scheme are: first, for the vertical coordinate to more closely follow an adiabatic surface on timescales that are short compared with the cutoff time $\tau_{\sim}$; and, second, to thereby minimize net spurious vertical advection of tracers. We note in passing that in an isopycnic model such as MICOM (Bleck & Smith, 1990), both of these hold by construction, and furthermore hold on all timescales. LM2011 demonstrated the effectiveness of $z^{\sim}$ by implementing the scheme in an idealized channel model, and energizing internal waves

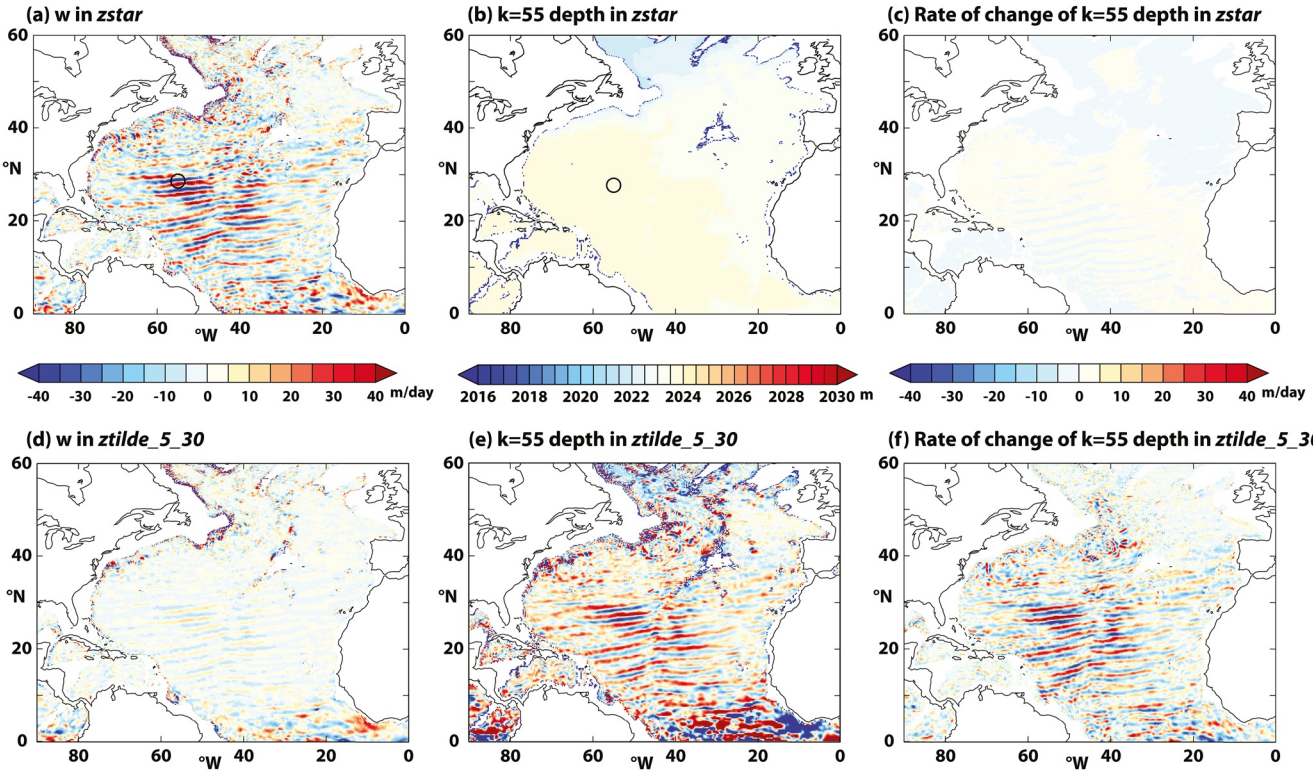

Figure 1. (a) The Eulerian vertical velocity w in m day^{-1} at level $k = 55$ with nominal depth closest to 2,000 m in *zstar*; (b) the depth in m of level $k = 55$ surface in *zstar*; (c) the rate of change of depth in m day^{-1} of this coordinate surface in *zstar*; (d) The Eulerian vertical velocity in m day^{-1} at level $k = 55$ in *ztilde_5_30*; (e) the depth in m of level $k = 55$ surface in *ztilde_5_30*; and (f) the rate of change of depth in m day^{-1} of this coordinate surface in *ztilde_5_30*. The black open circles in panels (a and b) denote the location of the water column used for analysis.

with a monochromatic 12-hr period. In the present study, by contrast, the complexity of the bathymetry, coastlines and ocean dynamics in a global model make such a simple approach challenging: internal waves are naturally present on a spectrum of frequencies from the Coriolis frequency to the buoyancy frequency, and we might not expect a priori to find waves with appropriate frequency and monochromaticity to use in comparably meaningful tests to those described in the above paper. However, Blaker et al. (2012) have noted that, in a similar NEMO implementation with the same horizontal resolution, NIGWs are created at northern and western boundaries and propagate in an equatorward and slightly eastward direction across subtropical gyres. These have periods a few percent shorter than the inertial period at any given latitude, which is close to 12 hr at 55°N, increasing to about 30 hr at 20°N. The waves have a vertical structure at this resolution that is typical of the first baroclinic mode, and in the western half of the North Atlantic between 25° and 45°N they have maximum vertical velocities at depths between 1,000 and 3,000 m of up to 50 m per day.

We shall use the NIGWs discussed above as a testbed to examine the performance of the model with respect to both of these objectives, and also to investigate the sensitivity of any improvements to the two timescale parameters in the $z^{\sim}$ scheme. More specifically, we focus on a location in the subtropical North Atlantic where the amplitude of the waves is typically high: we select a water column at $i = 930$, $j = 798$, located at 55°W, 28.5°N, and on the vertical level $k = 55$, which has a nominal depth in z^* of 2,101 m (see location marked in Figure 1). We shall refer to the vertical velocity defined at a given coordinate level, which in the model advects tracers across the coordinate surface, as the Eulerian vertical velocity. First, we compare the Eulerian vertical velocity with the rate of change of the coordinate depth at the same position: if $z^{\sim}$ is working as designed, it should at least partially replace the Eulerian vertical velocities associated with the NIGWs with coordinate displacements. Second, we compare the displacements of the coordinate surface with those of the potential density $\sigma_2 = 36.955$ kg m^{-3} surface, selected to lie close to the nominal depth of the $k = 55$ level in the same water column, and which should therefore be a good approximation to a neutral surface at this location. For metrics evaluated at a single time, we

shall use the mean over the first hour of the analysis period, namely the start of January 1996; for time series, we show hourly means during the first month of this period.

3.2. Diffusivity Estimate From Water Mass Transformation Rate

The analysis, based on that of Lee et al. (2002), is identical to that described in A. Megann (2018) and used again in MS2021. For clarity, we shall briefly define in this section the main quantities that we shall evaluate in Section 4.

A zonally integrated water mass transformation streamfunction $G(\Theta, \rho)$ is defined as

$$G(\Theta, \rho) = \Psi(\Theta, \rho) + \frac{\partial}{\partial t} V(\Theta, \rho) \tag{1}$$

where $\Psi(\Theta, \rho)$ is the overturning streamfunction at latitude Θ and potential density ρ, and $V(\Theta, \rho)$ is the volume south of Θ and below the isopycnal surface ρ. Considering only the ocean interior (defined as those regions in density space with potential density higher than the maximum surface density over an annual cycle), and assuming that the density transformation is entirely due to diffusive processes, which is a good approximation in water masses that are not directly subject to surface buoyancy forcing, we define a zonal mean effective diffusivity κ_{eff} as

$$\kappa_{\text{eff}}(\Theta, \rho) = \int_{\rho_{\max}}^{\rho} \frac{\partial G(\Theta, \rho)}{\partial y} d\rho \Big/ \int_{x_W}^{x_E} \frac{\partial \rho}{\partial z} dx \tag{2}$$

where x_W and x_E are the westward and eastward limits, respectively, of the basin at latitude Θ, and y is the northwards spatial dimension, both expressed in meters. The zonal integrals are carried out in density classes. We emphasize that this method makes no assumptions about equilibrium, since unsteadiness is accounted for in the second term on the right-hand side of Equation 1, but it does assume for the sake of simplicity that the longitude dependence of the integrands does not introduce unwanted effects, which reduces the robustness of comparisons between κ_{eff} and the explicit diffusivity κ_{exp}. In reality, as discussed by Lee et al. (2002) and by A. Megann (2018), there are additional contributions to the transformation rate from the nonlinearity of the equation of state, namely cabbeling and thermobaricity, but these tend to be spatially quite localized (mainly in the Southern Ocean and the subpolar North Atlantic: see Klocker and McDougall (2010)). The analysis we present here neglects these contributions, which tend to create negative values of the effective diffusivity in the latter regions.

We evaluate κ_{eff} in the same set of potential density σ_2 classes as used by A. Megann (2018) and by MS2021, from 5-day means from the final 10 years of the integrations (1996–2005), and compare this with the same quantity in the z^* experiment. In the experiments with $z^{\sim}$, the total effective meridional transport, which is the sum of the second order centered advective fluxes, an upstream corrective flux issued from the FCT scheme, and the "thickness diffusion" correction fluxes applied when the $z^{\sim}$ coordinate is updated, was used for the calculation of the streamfunction in place of the simple advective flux.

3.3. Basin Temperature and Salinity Biases

For $z^{\sim}$ to be an acceptable vertical coordinate for forced and coupled ocean configurations in realistic domains it should, overall, not increase biases in the temperature and salinity fields relative to observations, nor should it create new water masses that are not observed in the real ocean. If it reduces numerical mixing as intended, it should indeed tend to reduce the biases and drifts with respect to those found with z^*. We shall compare temperature and salinity censuses between the model experiments to confirm the first requirement, and present zonal mean temperature and salinity biases at selected depths with respect to climatological estimates to confirm the second condition. MS2021 demonstrated a strong correlation between the strength of the numerical mixing (quantified by the zonal and global means of the effective diffusivity κ_{eff}) in the closely related GO6 configuration, and the rate of cooling in the depth range 200–2,000 m in the globally averaged temperature: reduced mixing (in this case effected by raising the viscosity) was associated with reductions in the rate of drift by up to 50%, even though the picture was complicated by large-scale warm biases in the upper 200 m. This work also found that temperature and salinity biases of both signs at 300 m, a depth typical of the annual thermocline, were reduced (temperature more consistently than salinity) as the numerical mixing was reduced, and so we will directly

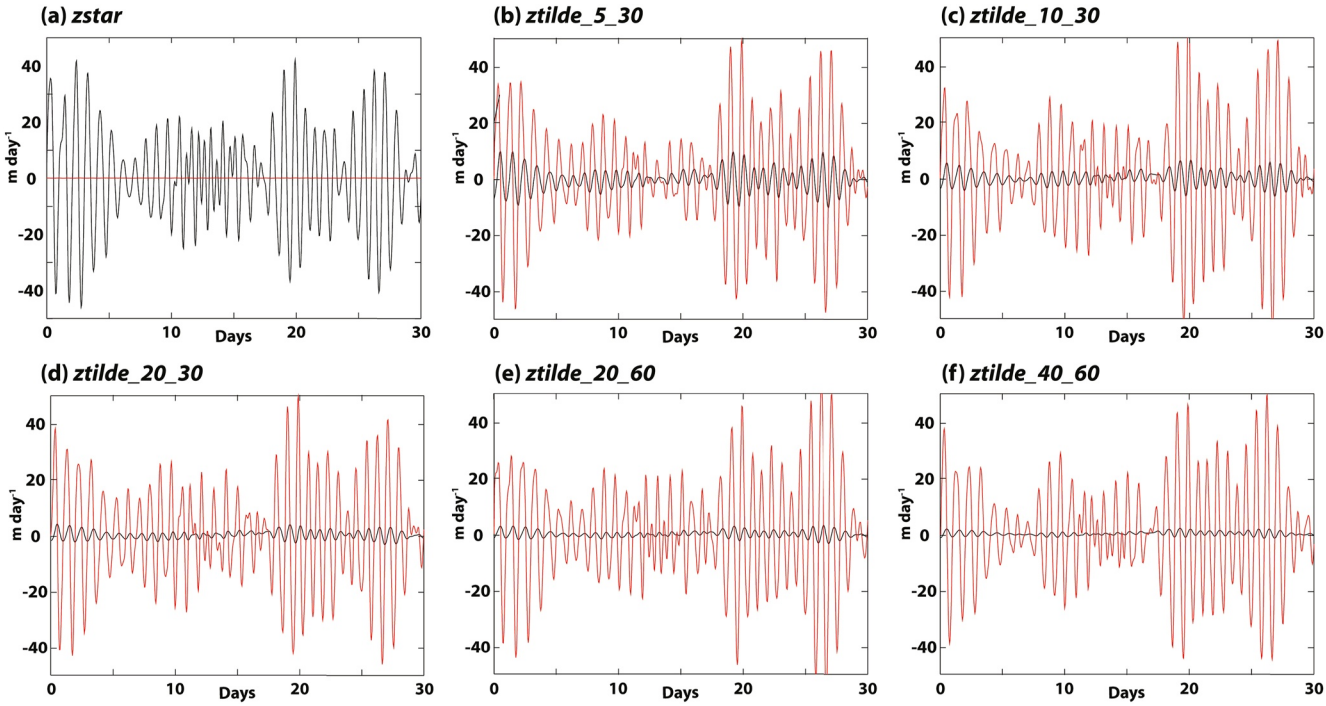

Figure 2. The Eulerian vertical velocity in m day^{-1} on the depth level $k = 55$ with nominal depth closest to 2,000 m (black lines) and the rate of change of depth in m day^{-1} of the same surface (red lines) in hourly means of (a) *zstar*; (b) *ztilde_5_30*; (c) *ztilde_10_30*; (d) *ztilde_20_30*; (e) *ztilde_20_60*; and (f) *ztilde_40_60*.

compare the dependence of the biases at this depth on $z^{\sim}$ and its time scale parameters with those resulting from increasing the viscosity.

4. Results

4.1. Vertical Coordinate Metrics

In the left-hand panels of Figure 1 we show the mean of the Eulerian vertical velocity on level $k = 55$, which has a nominal depth on the W grid of 2,023 m, in the first hour of the analysis period; the center panels show the depth of this level on the W grid, and the right-hand panels show the rate of change of the depth of the level in m day^{-1}, evaluated from consecutive hourly means. The top row of panels shows results from z^*, and the bottom panels results from the $z^{\sim}$ experiment with the default parameters, *ztilde_5_30* (see Table 1 for a list of model experiments). The black circle on Figures 1a and 1b indicates the location of the water column at 27.5°N, 55°W at which we shall quantitatively evaluate the time evolution of the wave fields in the following section. In the z^* case (Figure 1a), the NIGWs are represented clearly as vertical velocities with amplitudes of more than 40 m per day, and they have wavelengths of about 200 km and periods between 18 and 20 hr. In the $z^{\sim}$ case (Figure 1d), by contrast, the amplitude of the Eulerian vertical velocity is reduced by at least a factor of 5. The depth of the level $k = 55$ in the z^* case (Figure 1b) is, as expected, not affected by the vertical velocity, but with $z^{\sim}$ (Figure 1e) the imprint of the waves on the coordinate depth is clear, as are also that of the poorly resolved grid-scale features close to the topography at the western boundary and along the mid-Atlantic Ridge, and the internal waves close to the Equator (described in detail by Blaker et al. (2021)). Figures 1c and 1f show that representation of the NIGWs in the amplitude of the rate of change of the coordinate depth $z^{\sim}$ is very similar to that of the Eulerian vertical velocity field in z^*.

To evaluate more quantitatively the effect of $z^{\sim}$ on the model's response to large-amplitude internal waves, we focus on the water column at the location marked in Figure 1a. Figure 2 shows hourly means of the vertical velocity at this point on the same depth level $k = 55$, over the first month of 1996, overlain with the rate of change of the depth at this point, for z^* and the five $z^{\sim}$ experiments. The passage of trains of NIGWs with period of around 24 hr through this point is evident, with a modulation of the amplitude from very small values to more than

Table 2
Root-Mean-Squared Quantities Evaluated at 55°W, 27.5°N and at a Nominal 2,000 m Depth Over a Month of Hourly Means: The RMS Vertical Velocity; the Ratio of the Latter to That in the z Control Experiment; and the RMS Rate of Vertical Displacement of the Coordinate Surface*

Experiment	w_{RMS} (m day^{-1})	w_{RMS} fraction of w_{RMS} in z^*	$\partial z/\partial t_{RMS}$ (m day^{-1})
zstar	17.05	1.00	0.025
ztilde_5_30	3.752	0.22	17.74
ztilde_10_30	2.288	0.13	17.74
ztilde_20_30	1.373	0.08	17.74
ztilde_20_60	1.125	0.065	17.74
ztilde_40_60	0.6874	0.040	17.74

40 m/day over periods of between 10 and 15 days. The immediate impression given by Figure 2 is that, even with the default timescale parameters, the $z^{\sim}$ coordinate transfers most of the Eulerian motion in the z^* case into coordinate displacements, and that this process becomes more nearly complete as the $z^{\sim}$ timescales lengthen; in *ztilde_40_60*, the vertical velocity has been reduced almost to zero, while the time series of the rate of change of the coordinate depth is very similar to that of the vertical velocity in *zstar*. Table 2 lists the RMS value of these two quantities over the month, as well as the ratio of the RMS vertical velocity to that in *zstar*, and confirms these impressions, with a monotonic decrease in w_{rms} with lengthening timescales, the latter reaching in *ztilde_40_60*a fraction of only 4% of that in *zstar*. Since the filter timescale and the restoration timescale to z^* both act as first-order filters on the coordinate depths, we would expect that, as the respective timescales are increased, more of the wave spectrum is represented as an adiabatic quasi-isopycnal process in the model, instead of as a Eulerian velocity.

In Figure 3 we show time series of the depth anomaly of the $k = 55$ level at the same location (black solid lines); the depth anomaly of the $\sigma_2 = 36.955$ isopycnal (dashed black lines), which lies close to this depth at this location; and the difference between these time series (red lines), for hourly means over the same period as that shown in Figure 2. In the *zstar* case, the coordinate surface remains stationary, and the isopycnal surface ripples up and down at close to the inertial period as the trains of NIGWs pass through this water column, superposed on longer-timescale displacements from eddies and planetary waves. As the $z^{\sim}$ time scale parameters are lengthened, the isopycnal surface is displaced progressively less by the NIGWs: in *ztilde_5_30*, the maximum amplitudes of the ripples in the difference (red line) are of order 1–2 m, while in *ztilde_40_60*, they are between 0.3 and 0.5 m.

For accuracy and stability of the $z^{\sim}$ coordinate, we prefer that the deformation of the coordinate surfaces does not result in cell thicknesses that are too small. Figure 4 presents cumulative distributions of the ratio of the cell thickness in a single hourly mean of each cell to the thickness of the same cell in *zstar*, over selected depth

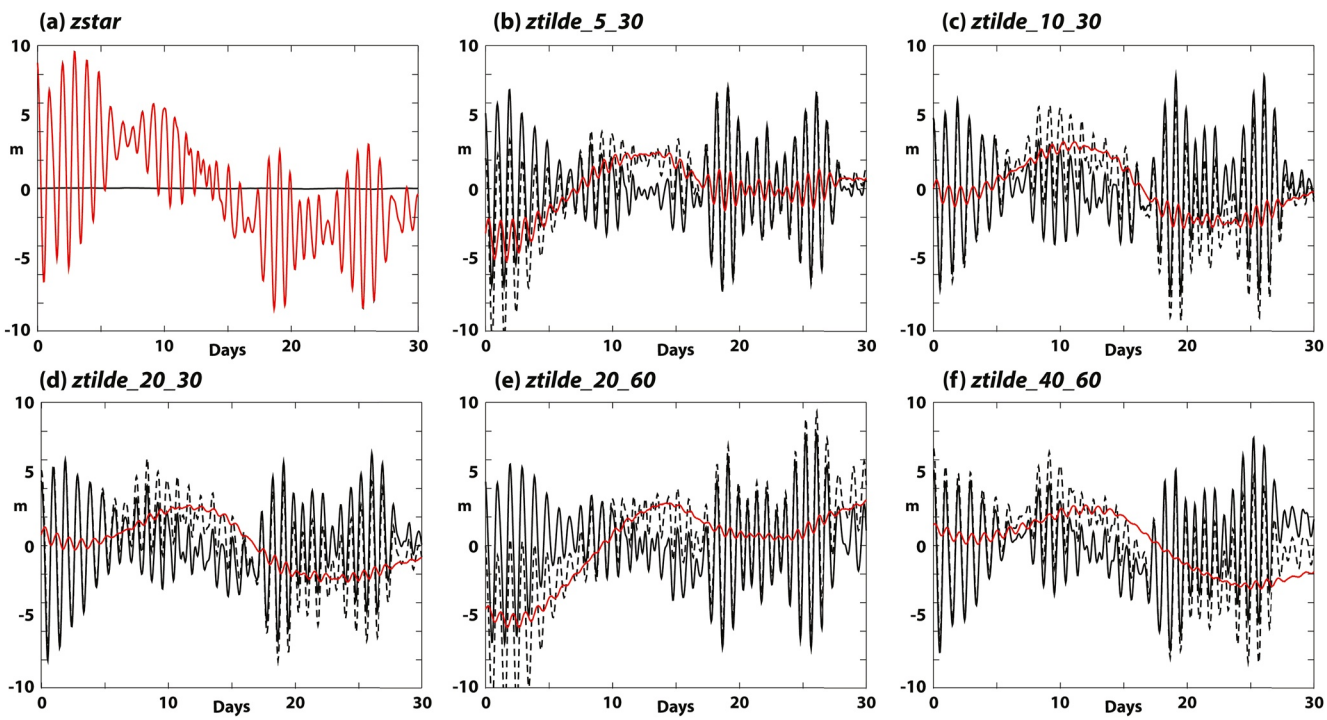

Figure 3. The hourly depth anomaly of the $k = 55$ coordinate surface (solid black lines), the depth anomaly of the $\sigma_2 = 36.955$ isopycnal surface (dashed black lines), and the difference between the two (solid red lines) in (a) *zstar*; (b) *ztilde_5_30*; (c) *ztilde_10_30*; (d) *ztilde_20_30*; (e) *ztilde_20_60*; and (f) *ztilde_40_60*.

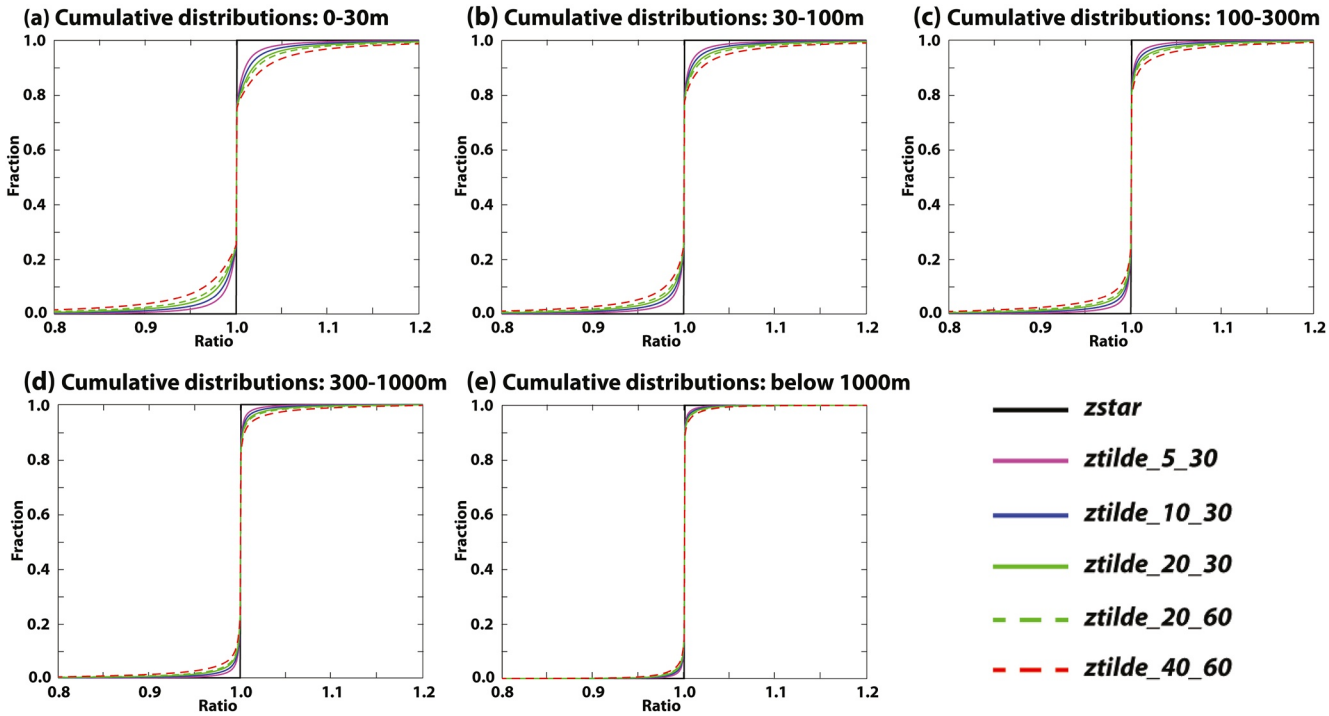

Figure 4. Cumulative histograms of the ratio of the cell thickness in the model experiments in the first hour of 1996 to the thickness of the respective cell in *zstar* in selected depth ranges: (a) 0–30 m; (b) 30–100 m; (c) 100–300 m; (d) 300–1,000 m; and (e) <1,000 m.

ranges. As might be expected, the widths of the distributions about a ratio of unity reduce with depth: the level thicknesses increase with depth (from 1 m at the surface, 100 m at 1,000 m depth, to 200 m at 5,000 m), while the displacements from internal waves will generally not increase in the same way. Figure 4 also confirms that in all depth ranges the displacements increase with the filter timescales in $z^{\sim}$.

Turning to stability concerns, the tails of these distributions are of interest: Table 3 lists the fraction of the ratio of the coordinate displacements in the model experiments in the first hour of 1996 to the thickness of the respective cell in *zstar*, in the same period, in the depth range 0–30m. We note first of all that there are no cells with a thickness less than a fraction 0.2 of the z^* thickness, so we conclude that vanishing cells are unlikely to occur with $z^{\sim}$ in this global domain. Second, almost all of the large ratios (>1.8) occur in water deeper than 3,000 m, rather than on the shelves, and even in the handful (fewer than 10) cases where a large ratio occurs in water shallower than 100 m it tends to be located toward the middle of the water column. Finally, ratios higher than 2.0 occur in a maximum of 8,844 grid cells (a fraction 6×10^{-5} of the whole domain) in *ztilde_40_60*, and fewer in all the other experiments. Problems with stability were not found with any of the $z^{\sim}$ integrations, so the fact that no vanishing cell thicknesses were seen implies that the rare occurrences of ratios higher than 2.0 is not likely to correspond to unphysical behavior.

Table 3
Fractions of the Model Grid Cells Where the Ratio of the Coordinate Displacements in the Model Experiments to the Thickness of the Respective Cell in zstar, in the Depth Range 0–30 m, Lies Within Specific Ranges (Top Row)

Experiment	<0.30	<0.40	>1.70	>1.9	>2.0
ztilde_5-30	0	1×10^{-5}	2×10^{-5}	3×10^{-6}	5×10^{-7}
ztilde_10-30	0	5×10^{-5}	9×10^{-5}	2×10^{-5}	4×10^{-6}
ztilde_20-30	0	16×10^{-5}	21×10^{-5}	5×10^{-5}	1.5×10^{-5}
ztilde_20-60	1×10^{-5}	38×10^{-5}	39×10^{-5}	8×10^{-5}	3×10^{-5}
ztilde_40-60	2×10^{-5}	85×10^{-5}	73×10^{-5}	16×10^{-5}	6×10^{-5}

Note. These are evaluated in the first hour of 1996.

4.2. Mixing Analysis

If $z^{\sim}$ performs as intended, and reduces the contribution of internal wave motions to numerical mixing, this should be quantifiable as a reduction in the rate of diffusive water mass transformation, evaluated as the effective diffusivity κ_{eff} as described in Section 3 and defined in Equation 2.

Figure 5 shows the ratios of the zonal mean of the effective diffusivity κ_{eff} to that in the z^* control *zstar* in each of the experiments, plotted against latitude and potential density σ_2. The black contours are of the overturning streamfunction, while the bold black dashed lines show the maximum monthly

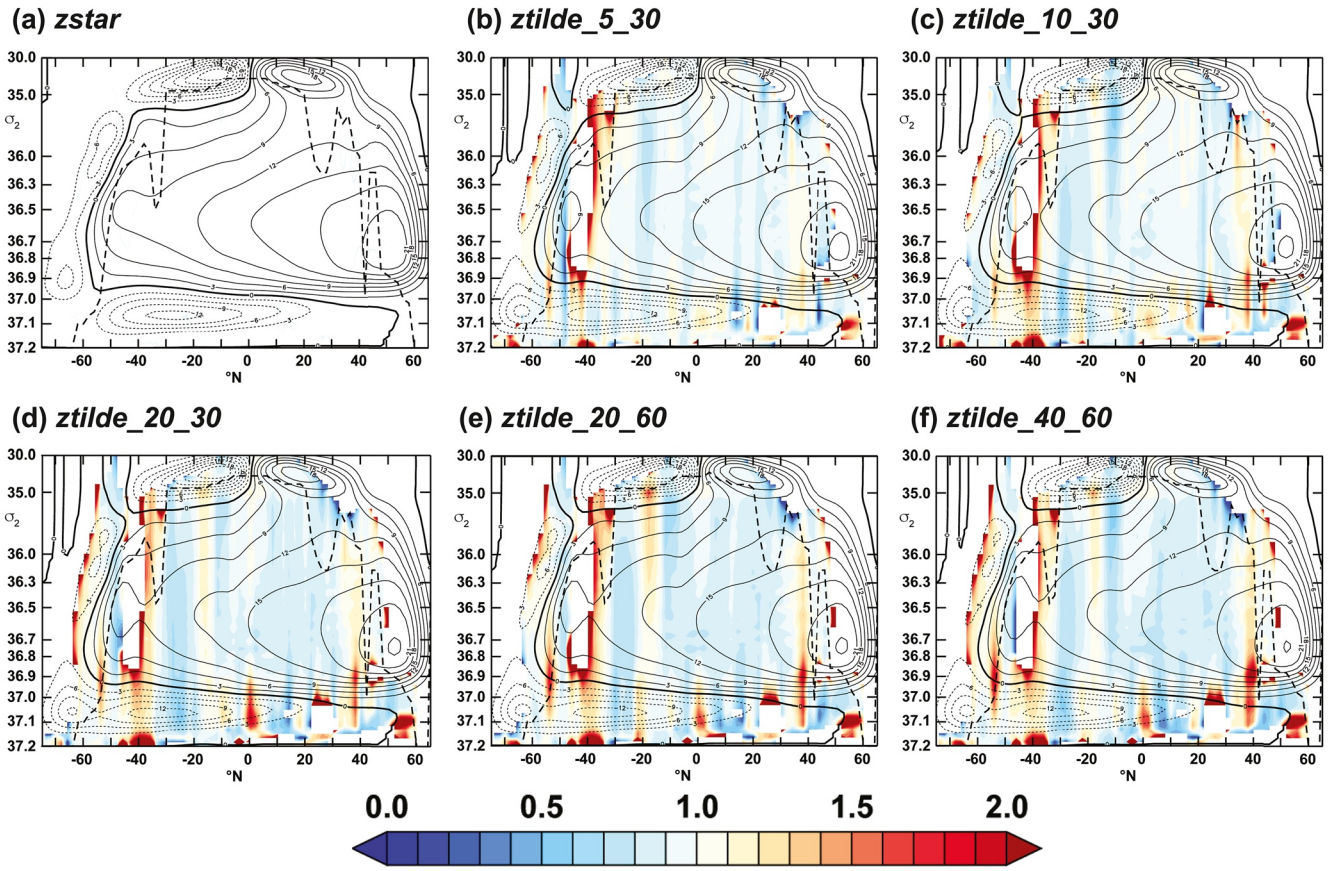

Figure 5. Ratios of the zonal mean effective diffusivity κ_{eff} to κ_{eff} in *zstar*, plotted against latitude and potential density σ_2 in (a) *zstar*; (b) *ztilde_5_30*; (c) *ztilde_10_30*; (d) *ztilde_20_30*; (e) *ztilde_20_60*; and (f) *ztilde_40_60*. Bold dashed contours denote the maximum surface density, and white regions correspond to negative diffusivities. Fine contours are of the overturning streamfunction, with dashed lines denoting negative values.

density in each latitude band over the 10-year analysis period, effectively delimiting the lower boundary of the surface-forced portion of density space over which Equation 2 no longer holds. The white areas in the interior correspond to negative values of κ_{eff}, which A. Megann (2018) ascribed to significant rates of density transformation due to cabbeling or thermobaricity: in particular, the negative diffusivities between 50° and 40°S lie in a region where these processes are thought to have a strong influence (e.g., Klocker & McDougall, 2010). The red coloring around the latter areas in Figure 5 is not significant, as it corresponds to κ_{eff} values crossing zero in *zstar*, and hence small values of the denominator of the ratio. It is clear that there is a consistent reduction in κ_{eff} (blue shading) over most of the domain in *ztilde_5_20* (Figure 5b), and that the reduction becomes stronger as the $z^{\sim}$ timescales are lengthened, although the similarity of panels (d–e) suggests that the effect starts to saturate with longer timescales. Apart from the aforementioned areas where small κ_{eff} values in *zstar* give high ratios, there are a few regions where $z^{\sim}$ gives only small reductions in effective diffusivity: there is little improvement in the upper ocean within 5°–10° of the Equator, and also a band around 20°S where $z^{\sim}$ appears to result in a small (5%–10%) increase in diffusivity in most density classes. There are also areas with high density characteristic of Antarctic Bottom Water (AABW; $\sigma_2 > 37.0$ kg m^{-3}) where κ_{eff} is higher with $z^{\sim}$ than with z^*, particularly close to the Equator, but these may result from small sample sizes, rather than significant increases in mixing. Overall, therefore, the reduction in κ_{eff} with $z^{\sim}$ is robust and consistent across the range of timescales used in the ensemble.

Figure 6 shows profiles in potential density classes of (a) the global area-weighted means of the explicit diffusivity κ_{eff}; (b) the ratios of global mean effective diffusivity κ_{eff} to the respective explicit diffusivity κ_{exp}; and (c) ratios of global mean κ_{eff} in each experiment to κ_{eff} in *zstar*. For the sake of clarity, results are not plotted for values of σ_2 lighter than 33.00 or denser than 37.05 kg m^{-3}. Finally, Figure 6d is a scatter plot of volume-weighted global means of κ_{eff} against an effective timescale defined as the geometric mean of the two timescales $\tau_{\sim}$ and τ_z. It can be seen in Figure 6a that the sensitivity of the explicit diffusivity to the $z^{\sim}$ parameters is small (changes of less

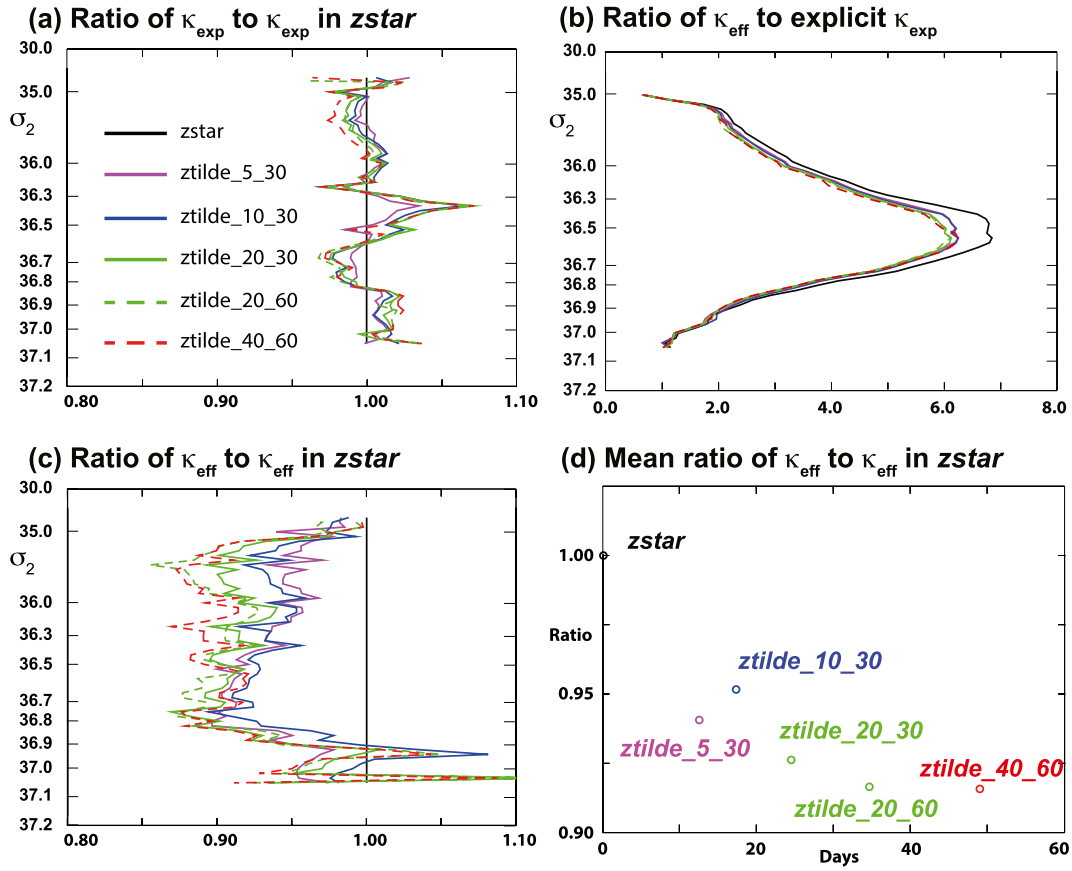

Figure 6. Ratios of global area-weighted mean effective diffusivities, evaluated in potential density classes, in the model ensemble: (a) ratio of global mean explicit diffusivity κ_{exp} to κ_{exp} in *zstar*; (b) ratio of effective diffusivity κ_{eff} to the respective explicit diffusivity κ_{exp}; and (c) ratios of κ_{eff} to κ_{eff} in *zstar*. (d) Scatter plot of the ratio of the mean κ_{eff} to κ_{eff} in *zstar* over the density range $35.50 < \sigma_2 < 36.9$ kgm^{-3}, against the geometric mean of the two $z^{\sim}$ timescales (defining this to be zero for the *zstar* experiment).

than 1%–2%) at most densities, with the exception of a consistent tendency for longer timescales to give a higher diffusivity in the density range between $\sigma_2 = 36.2$ and 36.6 kg m^{-3} (typically lying between the southward flowing deep waters and the overlying intermediate waters). The maximum increase is between 3% in *ztilde_5_20* and 6%–7% in *ztilde_20_60* and *ztilde_40_60*. Examination of the zonal mean explicit diffusivity (not shown here) suggests that $z^{\sim}$ increases the explicit diffusivity predominantly between 40° and 50°S.

Figure 6b shows the ratios of the global mean effective diffusivity κ_{eff} in each experiment to the explicit diffusivity κ_{exp} in the respective experiment. The ratio of κ_{eff} to κ_{exp} is generally between around unity, and is a maximum at a density around $\sigma_2 = 36.50$ kg m^{-3}, again typically intermediate between those of southward-flowing deep waters and of intermediate waters. At this density the maximum ratio in *zstar* is about 6.8, while this falls to between 6.0 and 6.2 in the $z^{\sim}$ experiments, a reduction of between 9% and 12%. The ratios of the effective diffusivity κ_{eff} in each experiment to κ_{eff} in *zstar* (Figure 6c) show that there is a consistent tendency for $z^{\sim}$ to reduce κ_{eff} with respect to that in the z^* configuration at densities less than $\sigma_2 = 36.9$ kg m^{-3}, and that increasing the $z^{\sim}$ timescales generally leads to lower values of κ_{eff} over this density range. To quantify this sensitivity, in Figure 6d we plot the mean of the ratio of κ_{eff} to κ_{eff} in *zstar* over the density range from 35.50 to 36.9 kg m^{-3} (values are listed in Table 4) as a scatter plot against the geometric mean of the two timescales, assigning a timescale of zero for z^*. A reduction of around 5% is obtained with both *ztilde_5_30* and *ztilde_10_30*, and the ratio continues to

Table 4
The Global Mean Effective Diffusivity κ_{eff} in Each of the Experiments (Column 2), and the Ratio of κ_{eff} to That in zstar (Column 3)

Experiment	Mean κ_{eff}	Mean ratio to z^*
zstar	9.28×10^{-5}	–
ztilde_5_30	8.685×10^{-5}	0.9411
ztilde_10_30	8.831×10^{-5}	0.9496
ztilde_20_30	8.838×10^{-5}	0.9262
ztilde_20_60	8.584×10^{-5}	0.9165
ztilde_40_60	8.554×10^{-5}	0.9158

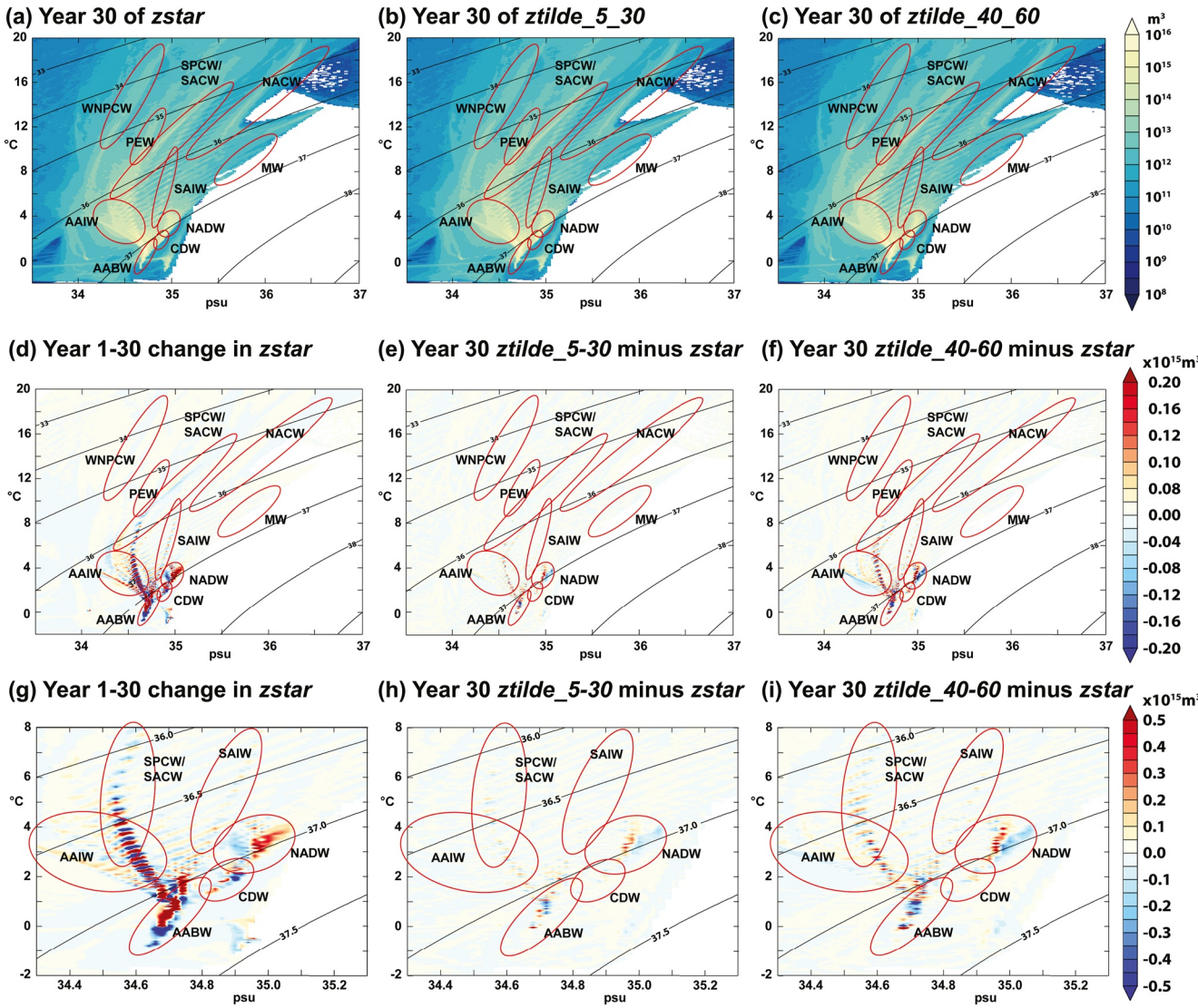

Figure 7. Water mass volume censuses: volumes in temperature and salinity classes in m^3 (on a logarithmic scale) in year 30 of (a) *zstar*; (b) *ztilde_5_30*; and (c) *ztilde_40_60*; (d) volume changes between year 1 and year 30 of *zstar*; (e) volume differences in year 30 of *ztilde_5_30* from those in the same year of *zstar*; and (f) volume differences in year 30 of *ztilde_40_60* from those in *zstar*. Panels (g–i) are identical to panels (d–f), but focus on the densest water masses, and these are shown on a narrower color scale. Red ellipses indicate approximate T/S ranges of selected water masses (the acronyms are expanded in the text), and black lines are contours of potential density σ_2.

decrease as the timescales are lengthened, but little improvement is seen between *ztilde_20_60* and *ztilde_40_60*, suggesting that any further lengthening of the timescale parameters is not worthwhile.

Comparison between Figure 6c and the corresponding Figure 7c in MS2021 reveals that the reductions in κ_{eff} obtained by implementing $z^{\sim}$ are of the same order as those resulting from increasing the biharmonic viscosity: doubling the fixed viscosity with respect to the default value or using the largest value of the Smagorinsky parameter $C_{\text{MSmag}} = 4$ both gave reductions of about 10%, although tripling the fixed viscosity reduced the effective diffusivity further than any of the $z^{\sim}$ settings.

4.3. Model Drifts and Biases

We have shown in the previous section of this paper that the $z^{\sim}$ coordinate reduces numerical mixing, as diagnosed by the zonal mean effective diffusivity based on large-scale density transformations, and to an extent that is comparable to that found with increased diffusivities by MS2021. We would, therefore, expect $z^{\sim}$ to have a

qualitatively similar effect in reducing drifts and biases in the interior temperature, and possibly to a lesser extent in the salinity, to those seen in simulations with higher viscosities. In this section we shall compare the sensitivity of changes in tracer fields to $z^{\sim}$ and its timescale parameters.

We first examine the sensitivity of property changes of the major water masses to the $z^{\sim}$ parameters. If enabling the $z^{\sim}$ coordinate results in changes to the large-scale temperature or salinity fields, we would require that the changes resulting from $z^{\sim}$ act to oppose those seen in the drift in the control. Panels (a–c) of Figure 7 show global water mass volume censuses in m^3 in year 30 of *zstar*; *ztilde_5_30* and *ztilde_40_60*: the temperature and salinity discretization employed has fixed intervals of 0.05 K and 0.02 psu, respectively. The red ellipses in each panel of this figure indicate the approximate regions of the major water masses in temperature-salinity space, based on the analyses of Worthington (1981) and of Emery and Meincke (1986). These water masses are, in order of decreasing typical temperatures, Western North Pacific Central Water; North Atlantic Central Water; South Pacific Central Water; South Atlantic Central Water; Pacific Equatorial Water; Mediterranean Water; South Atlantic Intermediate Water; Antarctic Intermediate Water (AAIW); North Atlantic Deep Water (NADW); Circumpolar Deep Water; and AABW. The black contours are of potential density σ_2. The overall census is qualitatively similar after 30 years in each of the experiments, and the maxima in population in the T/S classes after 30 years still correspond acceptably to those observed. Panels 6(d-f) show, respectively, the volume changes in the same T/S classes between years 1 and 30 of *zstar*; the volume differences between years 30 of *zstar* and *ztilde_5_30*; and the volume differences between years 30 of *zstar* and *ztilde_40_60:* increased volume in any T-S cell relative to the volume in *zstar* is represented by red shading, and decreased volume by blue shading. Although it is not obvious with this color scale, the changes in the mode waters in the $z^{\sim}$ runs are of opposite sign to those of the drift in *zstar*: for example, AAIW has a tendency to cool in *zstar* (red shading at lower temperatures and blue shading at higher), while this tendency is reversed between *zstar* and *ztilde_5_30* and *ztilde_40_60*, with larger differences in *ztilde_40_60*. Larger drifts can be seen to occur in the intermediate, deep and bottom water masses, the latter representing considerably higher volumes than the mode waters: although some artifacts from the vertical discretization can be seen as patches of rapidly alternating sign, particularly in the near-vertical "beam" of AAIW in the center left of panel (g), some systematic features are visible. For clarity, panels (g–i) show the same changes as in panels (d)-(f), but with the region in temperature and salinity space enlarged to focus on the densest water masses. The clearest example is in NADW: in *zstar* (panel (g)), there is a drift to increased salinity, presumably through mixing with overlying waters, but this drift is opposed to a small extent in *ztilde_5_30* (panel (h)) and to a larger extent in *ztilde_40_60* (panel (i)). Similarly, the tendency to warming of central AABW in *zstar* is partially opposed in *ztilde_5_30* and in *ztilde_40_60*, with the latter having a substantially stronger effect. We conclude that $z^{\sim}$ does not cause any significant unphysical modifications in interior water mass characteristics; and what changes it does induce are first opposite in sign to the drifts in the $z^{\sim}$ integration, and second strengthen with longer $z^{\sim}$ timescales.

In Figures 8 and 9, we show the biases in the zonal mean temperature and salinity, respectively, over the period 1996–2005, interpolated vertically onto selected depth levels, with respect to the corresponding fields in the EN4 climatology, averaged over the same period and interpolated onto the same depth levels. We first discuss the biases in the *zstar* control. At the surface, there are large-scale warm biases in tropical and subpolar latitudes, with cold biases in latitude bands centered at 40°S and 30°N. Below the surface, the magnitude of the temperature biases increases, and the warm bias at in the tropics and subtropics is replaced by a cold bias that grows to a maximum at around 500 m then decreases with depth. There is a warm bias in the Southern Ocean at all depths that appears to be persistent in NEMO simulations at this resolution (Storkey et al., 2018; Williams et al., 2018). The large excursions north of 35°N are chiefly related to biases in the paths of the North Atlantic Current (NAC) and the separated Kuroshio: the former tends to lie too far south as far north as Grand Banks, while the latter lies 2°–3° further north than the observed location. South of 35°N, the simulations tend to be slightly too salty at the surface, and fresher at 300 and 500 m depth, with the bias then reducing with depth. North of 35°N, they are generally saltier than the observed ocean, at all depths, and the bias again shows complex features related to the circulation. Finally, there are distinct surface biases between 60° and 70°N in Figures 8 and 9 in all the experiments that do not change within the ensemble.

The effect of $z^{\sim}$ on the biases, shown by the differences of the curves in Figures 8 and 9 from the solid black lines, can be seen to be relatively small at most latitudes and depths, compared with the biases themselves. Nevertheless, in the latitude range between 35°S and 35°N, quite large changes can be seen in the temperature biases in the thermocline (300 and 500 m) that robustly act to reduce the magnitude of the biases of both signs (Figures 8b

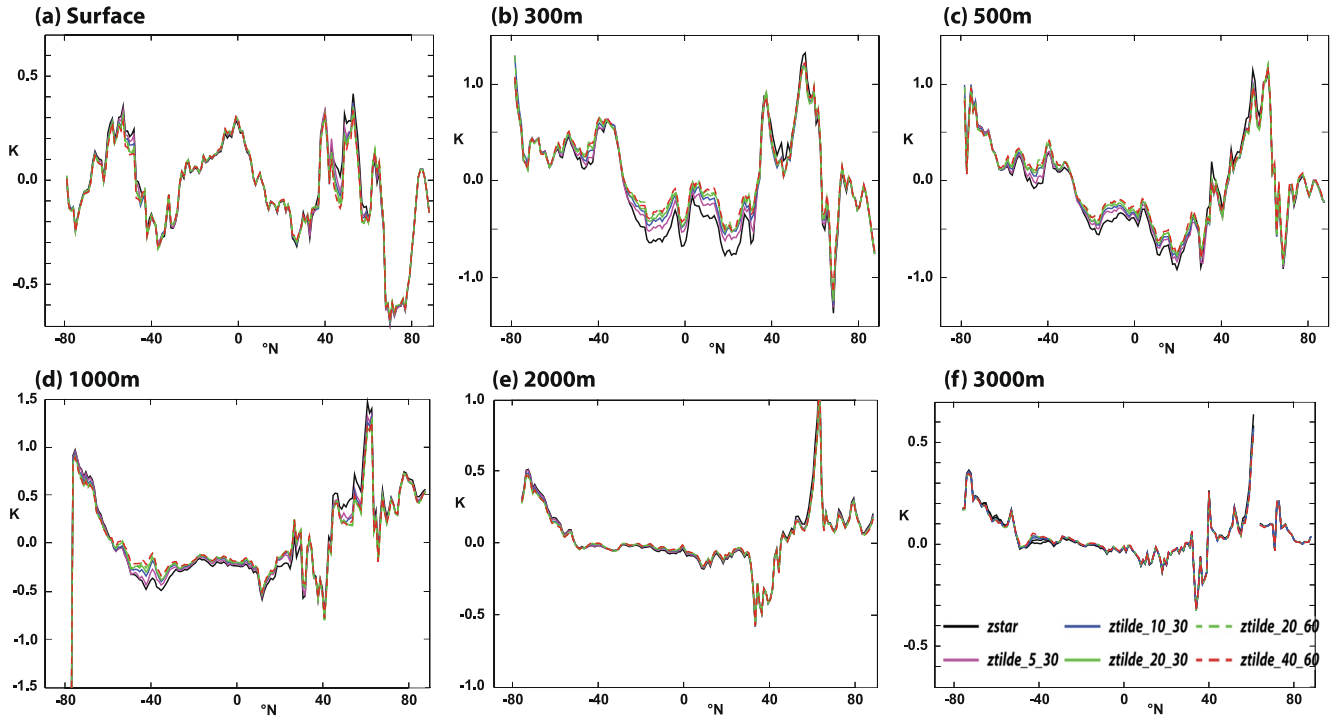

Figure 8. Zonal mean temperature biases in K of each of the experiments evaluated in 1996–2005, with respect to the EN4 climatology, at (a) the surface level; (b) 300 m; (d) 500 m; (d) 1,000 m; (e) 2,000 m; and (f) 3,000 m.

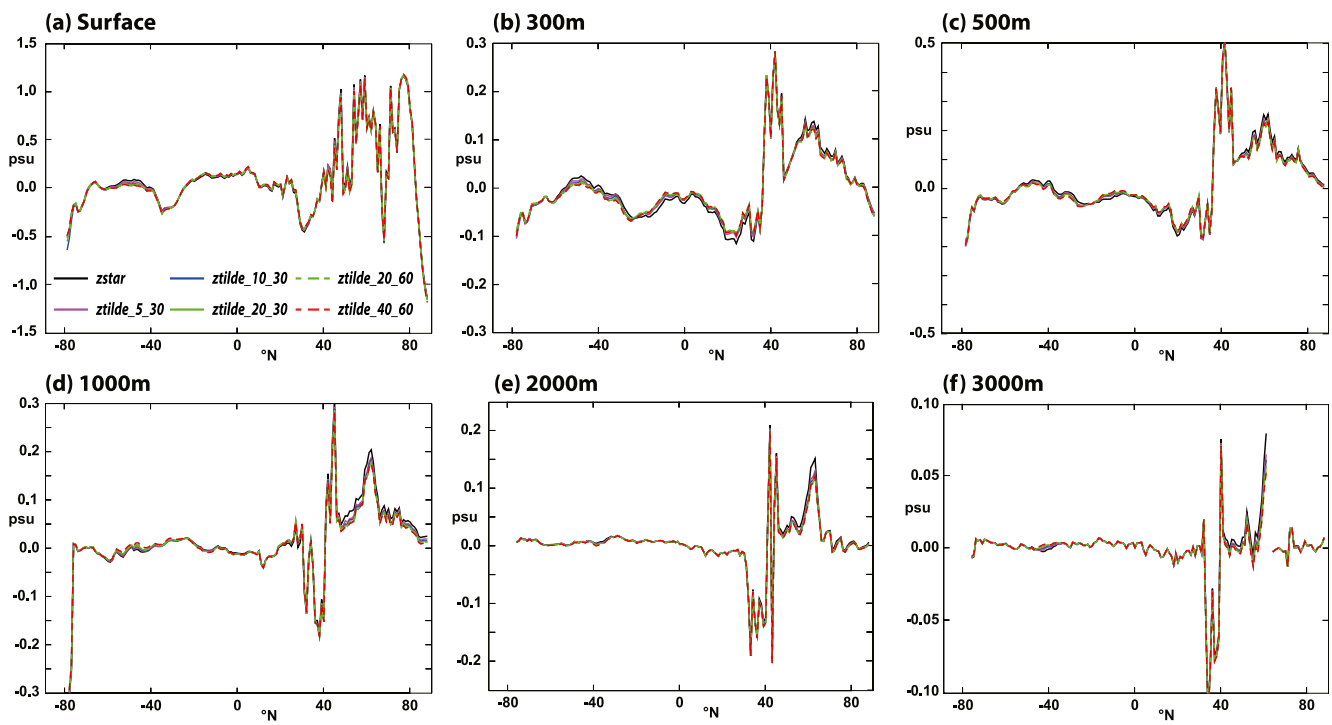

Figure 9. Zonal mean salinity biases in psu of each of the experiments evaluated in 1996–2005, with respect to the EN4 climatology, at (a) the surface level; (b) 300 m; (d) 500 m; (d) 1,000 m; (e) 2,000 m; and (f) 3,000 m.

Table 5
RMS Temperature Biases in K in 1996–2005 of Model Experiments at Selected Depth Levels, With Respect to the Same Period in the EN4 Climatology, With the Final Column Showing the Percentage Difference in RMS Bias Between zstar and ztilde_40_60

Depth (m)	*zstar*	*ztilde_5_30*	*ztilde_10_30*	*ztilde_20_30*	*ztilde_20_60*	*ztilde_40_60*	Change (%)
Surface	0.2387	0.2353	0.2813	0.2289	0.2276	0.2274	−4
300 m	0.5275	0.4760	0.4642	0.4471	0.4543	0.4461	−15
500 m	0.4805	0.4573	0.4458	0.4289	0.4286	0.4239	−12
1,000 m	0.3841	0.3629	0.3507	0.3473	0.3406	0.3431	−11
2,000 m	0.2332	0.2193	0.2133	0.2099	0.2089	0.2106	−10
3,000 m	0.1294	0.1225	0.1245	0.1213	0.1200	0.1204	−7

and 8c), and the effect increases monotonically with the $z^{\sim}$ timescales: at 300 m in particular, the cold bias reduces from between 0.3 and 0.6 K to 0.1–0.4 K, with about half the effect at 500 m. Similarly, north of 40°N and between 60° and 35°S, $z^{\sim}$ reduces the warm biases by up to 30%. $z^{\sim}$ has a smaller influence on warm biases at 1,000 m and deeper (Figures 8d–8f), but again it generally improves them. A consistent improvement can again be seen in the salinity biases, with the largest effect again seen at 300 m (Figure 9b); despite the improvements being at most of order 10%, the tendency is for all the $z^{\sim}$ curves to lie closer to zero than those for *zstar*.

To quantify the effect of $z^{\sim}$ on the model tracer fields, Tables 5 and 6 list the global RMS temperature and salinity biases at the same depth levels as those used in Figures 8 and 9, with the right-hand column showing the percentage difference in the RMS bias between *zstar* and *ztilde_40_60*. At every depth, applying $z^{\sim}$ reduces the global RMS bias in both temperature and salinity, and lengthening the $z^{\sim}$ timescale from the defaults leads to further reductions, with the proportional reduction in temperature bias typically about twice that in salinity.

The strongest sensitivity of the temperature biases to $z^{\sim}$ is seen at 300 m (Figure 8b), so to investigate the spatial distributions of the biases, we plot in Figure 10 the global temperature and salinity biases at this depth over the same period (1996–2005). As was the case with the experiments with increased viscosity described by MS2021 (Figures 10 and 11 of that paper), implementing $z^{\sim}$ with the standard parameters (Figures 10b and 10e) leads to a modest alleviation of the large-scale cold and fresh biases in the tropical and subtropical Atlantic and Pacific, while at the same time reducing the warm and salty biases in the North and South Pacific. Extending the $z^{\sim}$ timescales from *ztilde_5_30* to *ztilde_40_60* (Figures 10c and 10f) gives a further improvement in both temperature and salinity at this depth. The exception to this is in the subpolar North Atlantic, where a persistent cold bias over the path of the NAC develops with $z^{\sim}$ and worsens as the timescales are lengthened; this is associated with a southward and eastward displacement of the path of the NAC (not shown). The cold bias is likely to be a systematic error related to the 1/4° resolution: Marzocchi et al. (2015) found that in a comparable forced NEMO configuration, there was a large cold bias of up to 5K over the same region at 1° resolution, a cold bias over a reduced area at 1/4° and almost no large-scale bias at 1/12°.

Table 6
RMS Salinity Biases in psu in 1996–2005 of Model Experiments at Selected Depth Levels With Respect to the Same Period in the EN4 Climatology, With the Final Column Showing the Percentage Difference in RMS Bias Between zstar and ztilde_40_60

Depth (m)	*zstar*	*ztilde_5_30*	*ztilde_10_30*	*ztilde_20_30*	*ztilde_20_60*	*ztilde_40_60*	Change (%)
Surface	0.3755	0.3707	0.3688	0.3662	0.3673	0.3663	−2
300 m	0.1479	0.1413	0.1384	0.1373	0.1368	0.1373	−7
500 m	0.1209	0.1159	0.1146	0.1139	0.1136	0.1139	−6
1,000 m	0.0729	0.0700	0.0686	0.0674	0.0668	0.0667	−9
2,000 m	0.0493	0.0475	0.0471	0.0468	0.0467	0.0467	−5
3,000 m	0.0195	0.0189	0.0188	0.0186	0.0186	0.0185	−5

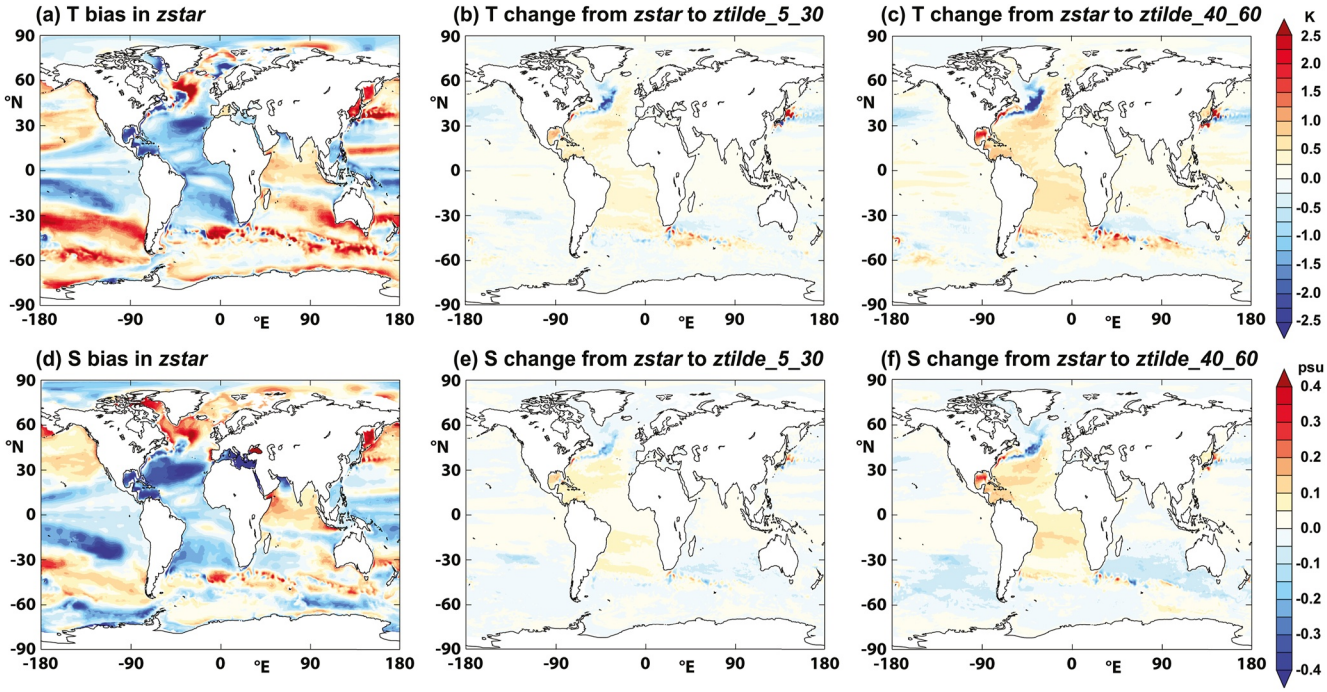

Figure 10. (a) Global temperature bias in K at 300 m in 1996–2005 with respect to EN4 in *zstar*; temperature differences from *zstar* in (b) *ztilde_5_30*; and in (c) *ztilde_40_60*; (d) global salinity bias in psu at 300 m with respect to EN4 in *zstar*; salinity differences from *zstar* in (e) *ztilde_5_30*; and in (f) *ztilde_40_60*.

4.4. Global Metrics

In this section, we discuss the sensitivity to $z^{\sim}$ of other metrics, including global mean quantities, large-scale circulation, the simulation of the Equatorial Pacific, and ice cover. Figure 11 shows time series of annual means of the volume-weighted global mean temperature and salinity, and of area-weighted surface fields, including sea surface temperature (SST), salinity, and surface heat and freshwater fluxes. First, we note that the dependence of these metrics on the $z^{\sim}$ parameters is robust, in the sense that where there is a significant sensitivity the ordering of values of the respective metric among the experiments is consistent for every year of the integration, and in addition that the ordering is invariably such that the difference from the *zstar* control increases monotonically with increasing timescale parameters. The mean temperature (Figure 11a) has the clearest sensitivity to the $z^{\sim}$ parameters: *zstar* (black line) shows a consistent cooling from 1900 onwards by about 0.1 K, which is reduced markedly by $z^{\sim}$, with the temperature drop from 1980 to 2005 reduced by 22% in *ztilde_5_20* and by 70% in *ztilde_40_60*, although the lack of representation of anthropogenic changes in longwave radiation in the CORE2 data set makes it difficult to comment on the relative realism of the temperature trends. The surface temperature (Figure 11b) reduces slightly with $z^{\sim}$ with further reductions with longer timescale parameters. The downward heat flux (Figure 11c) becomes less negative as the $z^{\sim}$ timescales are lengthened: the mean heat flux into the ocean from 1980 to 2005 increases by 0.21 Wm^{-2} from *zstar* to *ztilde_5_30* and by 0.59 Wm^{-2} from *zstar* to *ztilde_40_60*. We note that the ocean surface heat flux used here, "hfds," does not include latent heat from melting or freezing of sea ice, or from the geothermal heat flux. We may conclude that $z^{\sim}$ causes the model to lose less heat to the atmosphere; the only mechanism for this to happen, for a fixed surface forcing data set, is for the SST to be cooler, which appears to be the case, at least in the global mean; examination of the zonal mean SST in the ensemble (Figure 8a) confirms that the surface cooling occurs mainly in the latitude bands 40°–50°S and 35°–60°N.

The global mean salinity (Figure 11d) is not strongly dependent on $z^{\sim}$, with a slight tendency to increase at longer $z^{\sim}$ timescales, and the downward freshwater flux from precipitation and river runoff minus evaporation (Figure 11f) has no significant sensitivity to $z^{\sim}$: the only mechanism for a drift in the global mean salinity is then through the freshwater flux associated with surface salinity restoration (not included in the mean surface freshwater flux shown in Figure 11f), and this is confirmed by the opposite signs of the surface and depth-weighted mean salinity. As shown in Figure 9a, the surface salinity bias is slightly fresh at high latitudes, and salty in the

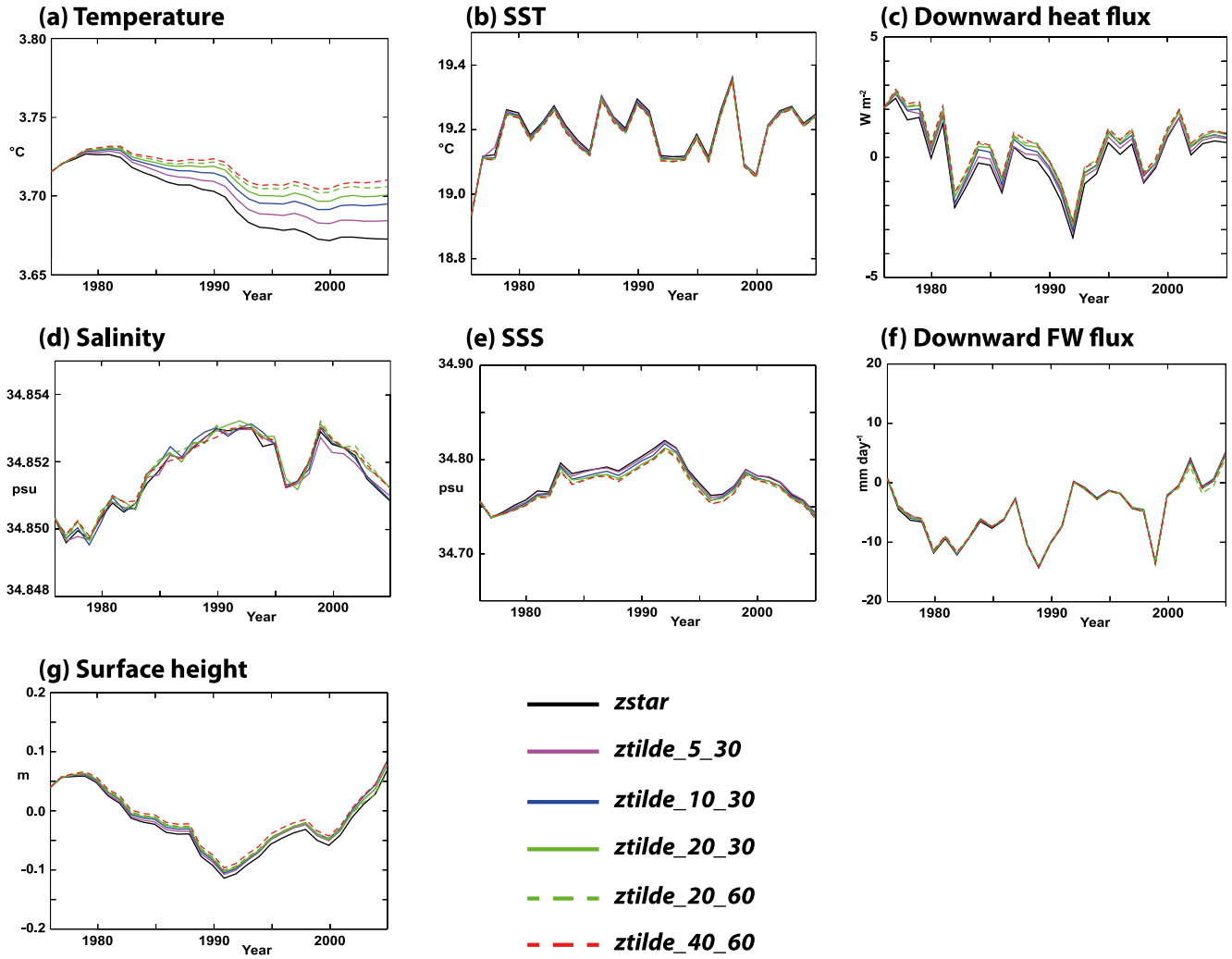

Figure 11. Global mean quantities as time series of annual means: (a) thickness-weighted mean temperature in °C; (b) surface temperature in °C; (c) surface downward heat flux in W m^{-2}; (d) thickness-weighted mean salinity in psu; (e) surface salinity in psu; (f) downward freshwater flux in mm day^{-1}; and (g) surface height in m.

tropics, consistent with a tendency to increased salinity stratification in the upper ocean, but we stress that this is only a weak effect. Finally, the SSH (Figure 11g), which does not include steric terms, is about 2 cm higher in *ztilde_5_20* than in *zstar*, but does not increase further in any of the other experiments.

Figure 12 shows the time evolution of the annual means of major large-scale transports in the model ensemble, including the Atlantic meridional overturning circulation (AMOC) strength at 26°N and at 45°N; the ocean heat transport (OHT) at 26° and 45°N; and the Antarctic Circumpolar Current (ACC) volume transport through Drake Passage. Table 7 lists the means of the above quantities over the period from 1996 to 2005, and the right-hand column lists the fractional change in the respective metric between *zstar* and *ztilde_40_60*.

As described by Storkey et al. (2018), the strength of the AMOC in the GO6 configuration was strongly dependent on horizontal resolution, being about 4 Sv higher at 1/12° than at 1/4°, and is unrealistically strong in both cases compared with observations (e.g., Smeed et al., 2018). The AMOC at 26°N in *zstar* (Figure 12a) follows a very similar trajectory to that of the 1/4° GO6 simulation, albeit about 3 Sv weaker, which may be a consequence of the different sea ice model in GO8p0.1. The overturning is significantly weaker with $z^{\sim}$ than with z^{*}, with a reduction of about 1 Sv between *zstar* and *ztilde_5_30* and a further reduction of 0.5 Sv as the timescales are lengthened, corresponding to a fractional weakening of 6% over the 10-year analysis period. It is not clear by which mechanism $z^{\sim}$ weakens the AMOC, but at the same time the reason why the latter is unrealistically strong in 1/4° NEMO simulations is not fully understood. The sensitivity of the AMOC at 26°N to $z^{\sim}$ is substantially

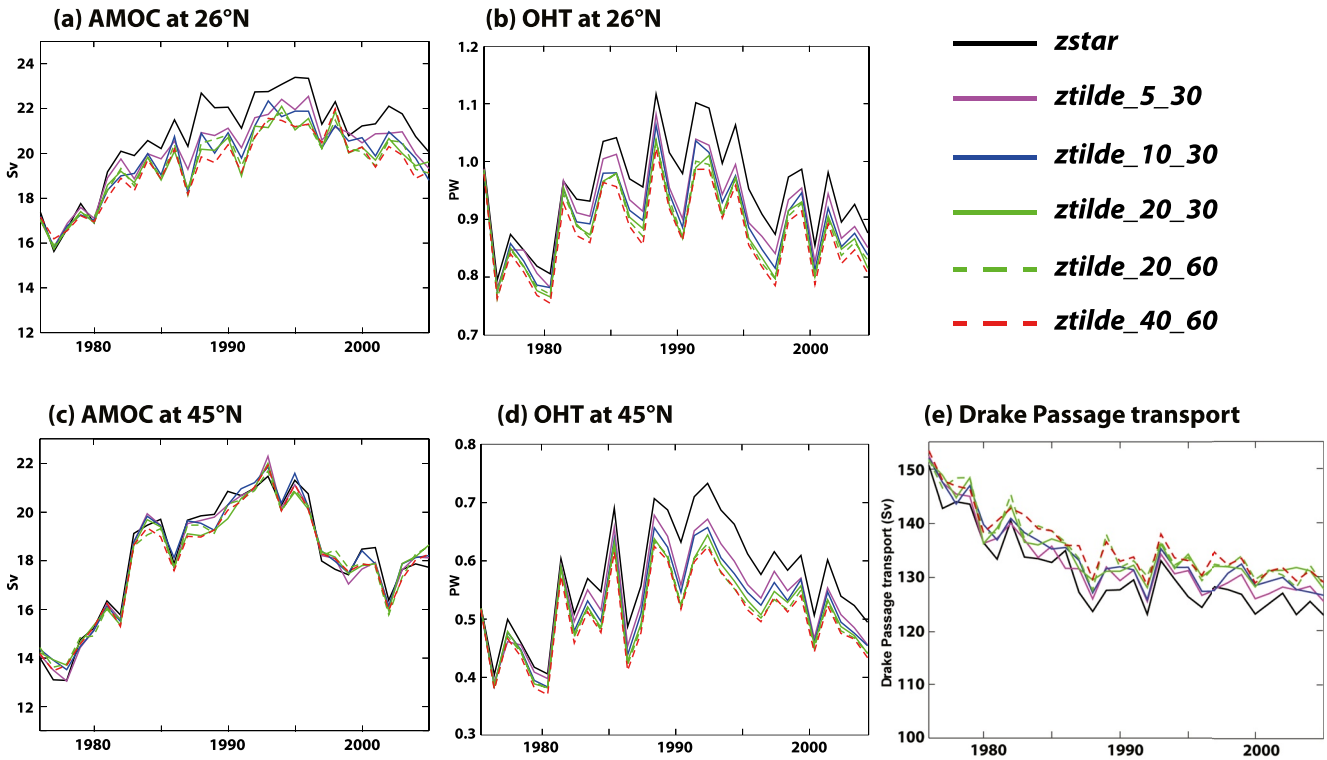

Figure 12. Large-scale transports in the model experiments: (a) Atlantic meridional overturning circulation (AMOC) strength in Sv at 26°N; (b) ocean meridional heat transport in PW at 26°N; (c) AMOC strength in Sv at 45°N; (d) ocean meridional heat transport in PW at 45°N; and (e) volume transport in Sv through Drake Passage.

stronger than that to increased viscosity, as observed by MS2021: in that study, only the experiment with the largest Smagorinsky viscosity showed a significant reduction in AMOC or OHT with respect to the control experiment. The large amplitude of the NIGWs at tropical and subtropical latitudes, as shown in Figure 1, would imply that the numerical diapycnal mixing from these could be substantial, and therefore amenable to mitigation by $z^{\sim}$, but a causal link between midlatitude mixing and the overturning circulation is not clear.

Although the OHT is primarily driven by the strength of the AMOC, it might be expected to be more sensitive than the AMOC to a reduction in mixing, since one would expect any increase in temperature stratification to result in a strengthening in the heat transport from an overturning circulation of a given strength. Looking at Figure 8, we see that at 26°N there is indeed a warming in the generally northward-flowing waters between 300 and 1,000 m in the $z^{\sim}$ experiments, relative to zstar, with very small temperature changes at the surface or below 1,000 m. Despite this, the OHT at 26°N (Figure 12b) reduces in *ztilde_40_60* by about 0.1 PW, or by about 10% of that in *zstar*. The OHT at 26°N in the *zstar* control is within the range of values calculated by Jackson et al. (2019) from a set of ocean reanalyses, but smaller than the 1.3 PW estimated by McDonagh et al. (2010), so

Table 7
Means From 1996 to 2005 of Transports in the Model Ensemble: Atlantic Meridional Overturning Circulation (AMOC) Strength at 26°N in Sv; Ocean Heat Transport (OHT) at 26°N in PW; AMOC Strength at 45°N in Sv; OHT at 45°N in PW; and Antarctic Circumpolar Current (ACC) Transport in Sv

	zstar	*ztilde_5_30*	*ztilde_10_30*	*ztilde_20_30*	*ztilde_20_60*	*ztilde_40_60*	Change (%)
AMOC at 26°N	21.50	20.78	20.45	20.34	20.22	20.18	−6
OHT at 26°N	0.9235	0.8875	0.8713	0.8586	0.8552	0.8431	−9
AMOC at 45°N	18.03	17.91	18.06	18.03	18.01	17.91	−0.6
OHT at 45°N	0.5657	0.5259	0.5157	0.5056	0.4987	0.4937	−13
ACC transport	125.3	127.5	128.6	130.6	130.7	131.1	+5

Note. The right-hand column lists the change in the respective metric between *zstar* and *ztilde_40_6*.

at this stage it is difficult to conclude that $z^{\sim}$ robustly makes the heat transport more or less realistic than in the control z^* simulation. Further north at 45°N, the AMOC strength (Figure 12c) is by contrast almost completely unaffected by $z^{\sim}$, but the OHT (Figure 12d) is again weakened by $z^{\sim}$.

The transport through Drake Passage (Figure 12e) does robustly increase as the $z^{\sim}$ timescales lengthen: after the second year, the transport is consistently between 5 and 10 Sv stronger in *ztilde_5_30* than in *zstar*, with that for the shorter timescales having intermediate values. This reduction of the rate of the unrealistic spindown of the ACC, relative to that seen in the standard 1/4° NEMO configuration, is similar to that reported as a result of increased viscosity by MS2021, who argued that suppression of grid scale noise in the velocity field would reduce the advection of momentum out of the ACC, but this is unlikely to be the mechanism acting here. Because of the strongly sloping isopycnals along the ACC, truncation errors in the horizontal tracer advection are likely to form a significant contribution to numerical mixing here, but the sensitivity noted in the present ensemble implies that $z^{\sim}$ indeed reduces the numerical mixing from vertical velocities associated with the vigorous eddy field in the Southern Ocean; this is evident in the *zstar* control as effective diffusivities κ_{eff} of more than five times the explicit diffusivity in density classes with $\sigma_2 > 36.5$ kg m^{-3} south of 45°S (see Figure 6a of MS2021).

4.5. Other Large-Scale Metrics

Holmes at al. (2021) found relatively high levels of numerical mixing in warm water classes within 10° of the Equator, particularly in the central and eastern Pacific, which they ascribed to a combination of large vertical and horizontal temperature gradients and noise in the velocity field at the grid scale, particularly in its horizontal components. MS2021 showed that, in the GO6 model configuration with default viscosity, some of the largest values of the cell Reynolds number were found between 10°S and 10°N, and that the effective diffusivity κ_{eff} was also relatively large in this region. In the top row of Figure 13 we show the standard deviation of the vertical velocity on an equatorial section in the Pacific down to 3,500 m depth in (a) *zstar*; (b) *ztilde_5_30*; and (c) *ztilde_40_60*. Consistent with our results for subtropical NIGWs in Section 4.1 and Figure 1, in *ztilde_5_30* the vertical velocity variation with time is reduced by about 35% with respect to that in *zstar*, and that in *ztilde_40_60* is reduced by between 70% and 80%. Nevertheless, the maximum vertical velocities are seen at a much deeper level than the equatorial thermocline, as represented by the 18°C isotherm, which in the present simulations slopes up from about 180 m at the west of the basin to about 70m at the east, so would not be expected to contribute significantly to numerical mixing at the thermocline, nor to affect the strength of the Equatorial Undercurrent (EUC). In Figures 13d–13f we show the temperature on the Equator in the upper 300 m in the same three experiments, and in Figures 13g–13i the zonal velocity over the same depth range, where the EUC is characterized by large eastward velocities close to the thermocline depth. There is a small expansion of the thermocline east of 120°W in the experiments with $z^{\sim}$, resulting in a cooling of about 1°C close to the surface and a comparable warming between 150 and 300 m, but nowhere below 500 m is there a temperature change of more than 0.05°C between *zstar* and *ztilde_40_60*. We conclude that $z^{\sim}$, although operating as intended to curtail the vertical velocities associated with high-frequency waves, has only a limited effect on mixing close to the Equator.

Reducing the level of mixing in regions covered by sea ice for at least part of the year might be expected to affect the seasonal ice cover: MS2021 found that increasing the viscosity led to a small alleviation of the unrealistically low ice cover in the Arctic, although even at the largest viscosities used in their study the summer ice extent was only increased by about 12% and still lay below the lower observational bound. Despite the change of sea ice model in the present configuration from CICE to SI^3, and despite the fact that only minimal tuning of the ice model parameters was carried out for this configuration, the seasonal cycles, and their biases with respect to the HadISST climatology, are very similar to those shown by MS2021. In contrast to the sensitivity of sea ice to viscosity found in the latter study, however, we find that $z^{\sim}$ has almost no effect on sea ice cover, nor on the sea ice volume: the NH 1996–2005 mean area changes by only −0.1% from *zstar* to *ztilde_40_60*; the mean NH volume by 0.7%; the mean SH area by +0.6%; and the mean SH volume by +2%. This is consistent with the zonal mean surface temperature bias shown in Figure 8a, where almost no spread between the experiments can be seen south of 60°S or north of 60°N.

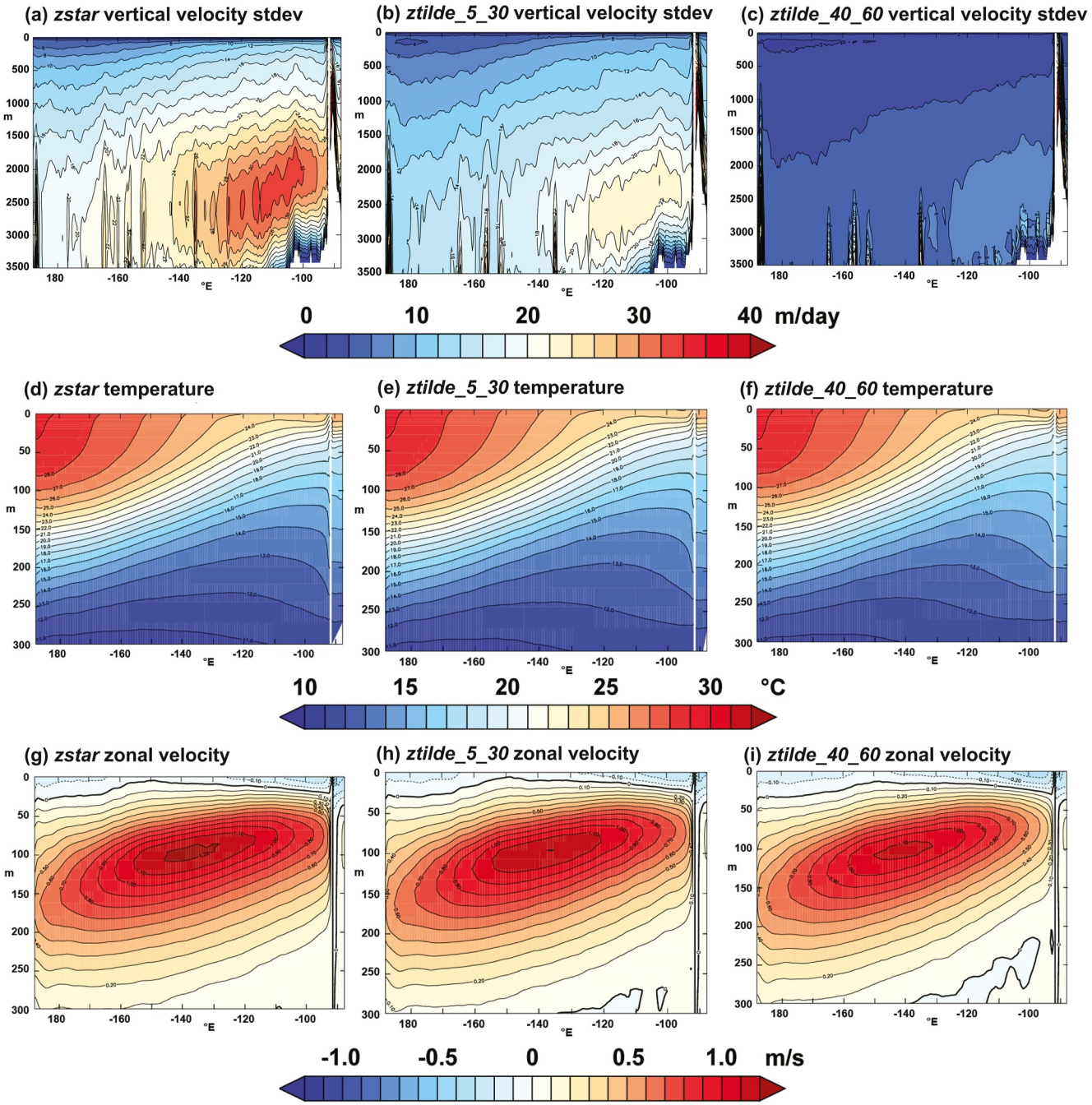

Figure 13. Standard deviation of the vertical velocity in m day^{-1} on an equatorial section in the Pacific in (a) *zstar*, (b) *ztilde_5_3,0*, and (c) *ztilde_40_60*; the temperature on the Equator in °C in the upper 300 m in (d) *zstar*, (e) *ztilde_5_30*, and (f) *ztilde_40_60*; and the zonal velocity in m s^{-1} over the same depth range in (g) *zstar*, (h) *ztilde_5_30*, and (i) *ztilde_40_60.*

5. Summary and Discussion

We have presented an assessment of the time-filtered $z^{\sim}$ vertical coordinate, using an ensemble of experiments based on a 1/4° global configuration of the NEMO v4 ocean model. The control experiment uses the default z^* fixed vertical coordinate, and the remaining five experiments use $z^{\sim}$ with different choices of the two timescale parameters in the $z^{\sim}$ scheme, namely the filter timescale $\tau_{\sim}$ and the timescale for restoration of the vertical coordinate depths to the fixed z^* depths τ_z; these vary from the default values of 5 and 30 days, up to 40 and 60 days, respectively. Lengthening these time scales permits vertical motions with increasingly long periods to

be represented as displacements of the vertical coordinate, rather than as advective vertical velocities with their potential to cause numerical mixing of tracers, and also, because of the low-order filter used in $z^{\sim}$, allows a larger portion of the wavelike behavior at any given frequency to be represented by the model as Lagrangian or adiabatic. The analysis is divided into three parts: first, we have assessed the sensitivity of the $z^{\sim}$ vertical coordinate to its timescale parameters in a single water column in the subtropical North Atlantic in the presence of NIGWs. Second, we have evaluated the effective diapycnal diffusivity, derived from density transformation rates, to quantify the effect of $z^{\sim}$ and its parameter settings on numerical mixing. Finally, we have investigated the realism of the simulation using a set of larger-scale metrics, including the representation and preservation of specific water masses; temperature and salinity drifts; large-scale circulation indices; the Equatorial Pacific; and hemispheric sea ice cover.

NIGWs are generated by wind power near the western boundaries of the subtropical gyres, with period close to the inertial period, and propagate eastward and equatorward. They are characterized by wavelengths of around 200 km and by vertical velocities of several tens of meters per day, and in 1/4° simulations they manifest chiefly as the first baroclinic mode. We have used a grid cell at around 2,000 m depth and in a location in the subpolar North Atlantic at 55°W and 27.5°N, where the NIGWs have consistently high amplitude, to investigate the effectiveness of $z^{\sim}$ in the present implementation in translating Eulerian vertical velocities into coordinate displacements, as well as assessing the sensitivity of this to the two timescale parameters. We have thereby confirmed that $z^{\sim}$ achieves two essential targets: first, it reduces the vertical Eulerian velocities associated with the NIGWs by a factor that increases from 3.5 with the default timescales to 15 with the longest timescales; and second, at this location the vertical coordinate at 2,000 m depth approaches increasingly closely the $\sigma_2 = 36.955$ isopycnal surface, which is close to being a neutral and adiabatic coordinate at this depth, as the timescale parameters are increased. In this sense, we have demonstrated that $z^{\sim}$ behaves increasingly like an isopycnal coordinate as the time scales are lengthened.

We have employed the mixing analysis of A. Megann (2018), evaluating an effective diffusivity κ_{eff} as a function of latitude and potential density σ_2 for each experiment as a metric of the overall diapycnal density transformation rate, which includes contributions from both explicit and spurious numerical mixing. We have compared the global mean of this with the explicit diffusivity κ_{exp} used in the model's mixing scheme, and with κ_{eff} in the z^* control: with z^*, the effective diffusivity κ_{eff} in density classes typical of intermediate and deep waters is between 4 and 8 times the explicit diffusivity, confirming the conclusions of previous studies that substantial numerical mixing occurs in this class of simulation. Lengthening the timestep parameters leads to progressive reductions in κ_{eff} by a maximum of around 10% in the two experiments with the longest timescales, confirming that $z^{\sim}$ reduces this contribution to numerical mixing, as intended.

If $z^{\sim}$ is to be useful in a global ocean model, it should first of all not create unphysical new water masses, and second tend overall to reduce biases in temperature and salinity, both on basin scales and more locally. Finally, it should not adversely affect the realism of large-scale circulation indices. We have shown here that all the major ocean water masses are preserved over the 30-year integration, and that where there are drifts, $z^{\sim}$ tends to reduce these, and increasingly so as the timescales are increased. We have demonstrated that zonal mean biases in salinity and temperature at selected depth levels are generally reduced by $z^{\sim}$, and at 300 m depth where the zonally averaged changes are strongest, they tend to consistently reduce the large-scale temperature and salinity biases, with again an increasing effect with longer timescale parameter values. The strength of the Atlantic overturning circulation at 26°N is reduced by up to 10% by $z^{\sim}$, which was deemed to represent an increase in realism, given the unrealistically strong transport in the z^* control, although the effect on the OHT was more equivocal, with $z^{\sim}$ leading to a reduction in an OHC in z^* that was already marginally weaker than that observed. Finally, a small reduction of the spindown of the volume transport through Drake Passage was seen in the $z^{\sim}$ experiments, consistent with a reduction in numerical mixing.

We have demonstrated that $z^{\sim}$ reduces the effective diffusivity κ_{eff} in the present 1/4° global configuration by up to 10%, provided that the timescales for this scheme are lengthened substantially beyond the default settings. This in fact implies a larger reduction than 10% in the rate of numerical mixing, since κ_{eff} includes the contribution from explicit mixing itself, so that the excess diffusivity is κ_{eff} minus κ_{exp}, and the proportion represented by the numerical contribution is $(\kappa_{\text{eff}} - \kappa_{\text{exp}})/\kappa_{\text{exp}}$. One might ask what the sources are of the remainder of the numerical mixing, and furthermore how these might be addressed. As we have already mentioned, using the default biharmonic viscosity of -1.5×10^{11} m^{4}s^{-1} has been found to give a simulation with persistent and widespread noise

at the grid scale (MS2021), and reducing the cell Reynolds number by increasing the viscosity (either by using a larger fixed viscosity parameter or by switching to the Smagorinsky deformation-dependent formulation), leads to reductions of a similar magnitude. Experiments with a combination of $z^{\sim}$ and tripled biharmonic viscosity (not presented here) have confirmed that the benefits of the two changes are additive. Other experiments with the same configuration (again not shown here) have shown that changing to a fourth-order horizontal tracer advection scheme gives further reduction in κ_{eff} by about 10%, and this improvement is again additive in combination with $z^{\sim}$; it is probable that the higher-order advection reduces truncation errors in the presence of a velocity field that is significantly noisy at the grid scale, and this would also be expected to reduce the projection of truncation errors in horizontal tracer advection into the dianeutral direction. The standard GO8 configuration uses the default Cox (1987) scheme for isoneutral diffusion, but other schemes are now known to more accurately align the mixing along the local neutral direction (Griffies et al., 1998) and therefore reduce undesirable dianeutral leakage. The scheme is available in NEMO 4.0: we would expect this to provide a further reduction in numerical mixing, but we have not systematically tested this in the present configuration. It is possible that a more accurate vertical tracer advection scheme than the second-order FCT used in the present simulations might reduce numerical mixing from vertical advection, but in the 1/4° GO8p0 configuration changing to fourth-order vertical FCT is found—perhaps surprisingly—to have a much lower effect than increasing the accuracy of the horizontal advection. Finally, numerical entrainment of overflow waters is likely to contribute, albeit in a relatively localized way, to numerical mixing: A. Megann et al. (2021) found that dense Arctic waters in a related global 1/4° configuration were unrealistically strongly mixed at the sills and did not penetrate significantly into the subpolar North Atlantic, nor did they contribute substantially to variability in the meridional overturning circulation at 26°N. The use of hybrid vertical coordinates, combining terrain-following coordinates over the shelf break with geopotential surfaces in the open ocean, to address this source of numerical mixing is being investigated in NEMO, and is already showing promising results (Bruciaferri et al., 2018; Wise et al., 2022).

LM2011 noted that, while computation of the pressure gradient on level geopotential surfaces in z^* configurations of NEMO was quite straightforward, the sloping coordinate surfaces in $z^{\sim}$ presented more of a challenge to the numerical solution, although they did not include any estimation of the pressure gradient errors in their simulations. The more rigorous techniques developed for terrain-following models (e.g., Shchepetkin & McWilliams, 2003) are becoming considered more appropriate for the NEMO model, particularly in the context of ongoing work on localized hybrid z^*-terrain-following coordinate systems for the sill overflow regions in the North Atlantic (Bruciaferri et al., 2018; Wise et al., 2022). The finite volume approach presented by Adcroft et al. (2008), unlike the former schemes, in addition specifically addresses the thermobaric instabilities that can arise when the coordinate system moves in response to the flow. These schemes are likely to offer benefits in cases using $z^{\sim}$, although evaluating the consequences of truncation errors in the pressure gradient calculation that are not based on residual spurious time-mean circulation will be more challenging.

In Section 4.1, we showed that the fraction of grid cells in our $z^{\sim}$ experiments where the change in the grid thickness from the $z^{\sim}$ scheme was larger than a few tens of percent of the thickness in z^* was less than 10^{-4}, although this fraction increased with longer $z^{\sim}$ timescales. Our analysis of the response of the vertical coordinate in the presence of NIGWs showed that these waves caused the largest change in thickness of up to 10 m at depths below 1,000 m, where the z^* level thickness in the model grid is at least 100 m, so the relative distortion in this regime, at least, is small. Nevertheless, Petersen et al. (2015) sounded a note of caution, reporting that, in their lock exchange experiments using z-tilde in the MPAS-Ocean model, significant distortion to the grid cells occurred, resulting in excessive numerical mixing. This is unlikely to be the case in the global domain we have described on a 1/4° grid, but where higher resolutions may permit more energetic vertical coordinate displacements it would be prudent to check that undesirable grid distortions do not occur to any significant extent.

In summary, the $z^{\sim}$ coordinate, as implemented in the NEMO v4 branch we have used, performs as intended, and leads in general to an improvement in model realism, in particular reducing model drifts and the rate of spin-down of the ACC. However, we have demonstrated that the default settings of the $z^{\sim}$ timescale parameters of 5 days for $\tau_{\sim}$ and 30 days for τ_z result in only relatively small improvements, whereas lengthening both of these to 40 and 60 days, respectively, strengthens its operation with no adverse effects. The numerical mixing resulting from inertial waves is likely to be more sensitive to the choice of the shorter of the two timescales (in this case $\tau_{\sim}$), even though small improvements are still visible (notably in Figures 2d, 2e and 6d) between the *ztilde_20_30* and *ztilde_20_60* experiments where only τ_z is changed. The effect of $z^{\sim}$ appears to start to saturate in the two experiments with the longest time scale parameters, so there is unlikely to be an advantage in lengthening them

further. The only significant drawbacks from $z^{\sim}$ in this configuration are the increase of between 15% and 20% in run time relative to the standard z^* case, and an increase in the cold bias in the north-western Atlantic, as shown in Figure 10, although the latter is likely to be a consequence of a systematic error in the path of the NAC at the present resolution (e.g., Hirschi et al., 2020), rather than a bias introduced directly by $z^{\sim}$. We may therefore recommend it, albeit with specific minor reservations, as a tool to reduce numerical mixing in 1/4° global simulations. At higher resolutions, where the amplitudes of vertical velocities associated with internal waves, eddies and equatorial waves are likely to be substantially larger than at 1/4°, and also particularly in simulations with tidal forcing, its benefits in reducing numerical mixing are likely to be proportionally larger, and the degradation in run speed from $z^{\sim}$ may well be regarded as a negligible disadvantage.

Appendix A: Summary of the $z^{\sim}$ Scheme

We first summarize the formulation of the LM2011 $z^{\sim}$ vertical coordinate, and then describe some practical modifications applied to the latter scheme to improve its robustness in the present global configuration.

A1. Summary of the LM2011 Scheme

In the following, the vertical discretization is defined in terms of layer thicknesses $e_3 = \partial_k z$ where z is the local depth (increasing downwards) and k refers to the vertical direction. The layer thicknesses are constrained such that their vertical sum must equal the total depth $(H + \eta)$ where H is the total depth at rest and η is the sea surface height. They should also preferably be not too small (infinitesimally small, "vanishing" layers being not supported in Nucleus for European Modeling of the Ocean [NEMO]) and not exhibit strong lateral variations for the sake of numerical stability.

Before turning to the $z^{\sim}$ scheme, it is worth introducing the usual, quasi-Eulerian, vertical coordinate in NEMO, the so called z^* coordinate (Adcroft & Campin, 2004). It simply states that the η tendency is distributed proportionally to the thickness fraction as follows:

$$\partial_t e_3^* = \frac{e_3^*}{H+\eta}\partial_t \eta = -\frac{e_3^*}{H+\eta}\int_{k_b}^{k_t} D\,dk = -D^* \tag{A1}$$

We have here introduced the flow divergence $D = \nabla_h \cdot \left(e_3^* \boldsymbol{u_h}\right)$ with $\boldsymbol{u_h}$ being the horizontal velocities, neglecting freshwater sources and sinks for the sake of simplicity. Initializing the model from what we will call a background "reference" Eulerian vertical coordinate system at rest e_3^0, one can show that Equation A1 reduces to $e_3^* = e_3^0/H(H+\eta)$ at each model time step. This formulation has the advantage that it ensures perfect tracer conservation, provided that certain changes are made to the forcing and filtering terms in the leapfrog time stepping scheme, as described by Leclair and Madec (2009).

The $z^{\sim}$ coordinate is built over the z^* coordinate by considering in addition internal variations of thicknesses e_3':

$$\partial_t e_3^{\sim} = \partial_t e_3^* + \partial_t e_3' \tag{A2}$$

The only constraint here is that the vertical sum of $\partial_t e_3'$ must be 0. It is worth pointing out that the implementation of $z^{\sim}$ described by Petersen et al. (2015) in MPAS has a slightly different definition of the η contribution:

$$\partial_t e_3^{*\mathrm{MPAS}} = \frac{e_3^0}{H}\partial_t \eta = \frac{\left(e_3^{\sim} - e_3'\right)}{H+\eta}\partial_t \eta \neq \frac{e_3^{\sim}}{H+\eta}\partial_t \eta; \tag{A3}$$

this is therefore different compared to the original LM2011 scheme, transferring part of the barotropic heave into the e_3' equation. This has the advantage of preventing potential slow drift of e_3^*, as discussed in the next section.

To obtain a fully Lagrangian coordinate, one can write:

$$\partial_t e_3' = -\left(D - D^*\right) = -D', \tag{A4}$$

which from the continuity equation, $\partial_k w = -D - \partial_t e_3^{\sim}$, and Equation A2 obviously leads to zero cross-layer velocities w.

LM2011 proposed a definition of e'_3 such that only high frequency motions are treated in a Lagrangian way, the vertical coordinate reverting to the e^*_3 system at low frequencies. In order to do so, they introduced a "low frequency" divergence D^{LF} obtained through a first-order filter of the baroclinic divergence D', which is applied as an additional source term in Equation A4. Since this does not prevent the long-term drift of e'_3 away from zero, a relaxation term is necessary. Finally, some regularization of the coordinate thanks to a Laplacian filtering of the anomaly is introduced. The LM2011 scheme can be summarized by the following set of equations:

$$\partial_t e'_3 = -D' + D^{\mathrm{LF}} + \nabla_h \cdot \left(\kappa_h \nabla_h e'_3\right) - \frac{2\pi}{\tau_z} e'_3 \tag{A5-1}$$

$$\partial_t e^*_3 = \frac{e_3}{H+\eta}\partial_t \eta = -D^* \tag{A5-2}$$

$$\partial_t D^{\mathrm{LF}} = -\frac{2\pi}{\tau_\sim}\left(D^{\mathrm{LF}} - D'\right) \tag{A5-3}$$

Equations A5-1 and A5-2 are discretized in time following the three-time-level leapfrog scheme used in the rest of the NEMO code (in other words, all of the terms on the RHSs are evaluated at the central time step, except for the diffusive and relaxation terms which are evaluated at the previous time step). Equation A5-3 is discretized according to a forward-in-time scheme, to avoid saving in memory an additional D^{LF} array, which basically translates into a first order exponential filter.

As a side note, one could have only implemented the restoration of the interfaces to z^* (τ_z, as in Gibson et al., 2017) but at the cost of reducing the filtering order for e_3.

A2. Modifications to the LM2011 Scheme

The LM2011 scheme has the merit of providing a clear framework to move from a quasi-Eulerian coordinate toward a fully Lagrangian one. However, the numerical implementation, as given in the latter paper, suffered from a number of issues listed below that made it unstable in realistic simulations.

A.2.1. Restoration to z*

There is no control of the possible drift of the e^*_3 in Equation A5-2. This effectively leads, in spite of the relaxation term in Equation A5-1, to a long-term evolution of e_3 that could be significantly different from e^0_3. To this end, Equation A5-2 is modified by adding a relaxation term:

$$\partial_t e^*_3 = -D^* - \frac{2\pi}{\tau_z}\left(e^*_3 - \frac{e^0_3}{H}(H+\eta)\right) \tag{A6}$$

which, for convenience, uses a time scale τ_z identical to the one used in the baroclinic thickness Equation A5-1. In the experiments presented here, we have followed the formulation of Petersen et al. (2015), for example, Equation A3.

A.2.2. Preserving Thicknesses Positivity

To prevent creating negative thicknesses, the $z^\sim$ coordinate is re-formulated in a similar way as for fully Lagrangian models: instead of time stepping the internal thickness anomaly Equation A5-1, the full thickness Equation A2 is used, e'_3 being this time deduced from Equation A2. Considering Equation A6 at the same time, Equations A5-1 to A5-3 becomes:

$$\partial_t e^\sim_3 = -\nabla_h \cdot \left(e^\sim_3 \boldsymbol{u_h}\right)_{FCT} + D^{LF} + \nabla_h \cdot \left(\kappa_h \nabla_h e'_3\right) - \frac{2\pi}{\tau_z}\left(e^\sim_3 - \frac{e^0_3}{H}(H+\eta)\right) + ORT \tag{A7-1}$$

$$\partial_t e'_3 = \partial_t e^\sim_3 + D^* \tag{A7-2}$$

The divergence tendency term in Equation A7-1 is here formulated as a second order advective term with a Flux Corrected Transport (FCT) scheme (Zalesak, 1979). Corrective diffusive fluxes are stored, as for thickness diffusion terms, and are used later on in the continuity equation (and tracer advection). Hence, these fluxes do not lead

to extra Eulerian cross-layer velocities. The last term in Equation A7-1 stands for "Other Regularization Terms" which are described as follows.

A.2.3. Vertical Regridding

A Lagrangian model would ideally treat solid lateral boundaries by inflating "sleeping" layers if required, a feature which is not allowed with the static masking used in NEMO (in other words, the number of wet vertical levels is fixed in time). This leads, in the particular case of tidal forcing, to potentially large variations of interfaces near the topography and, eventually, velocity interfaces crossing bottom steps. To deal with this boundary problem, a strong relaxation to the background Eulerian interfaces is applied near the bottom. At the same time, a minimum layer thickness of 1 m is ensured. This regridding step is implemented by scanning the column layer interfaces and importing volume from adjacent layers if necessary.

A.2.4. Conditional Smoothing

The constant thickness diffusion term in Equation A7-1 cannot prevent the occurrence of strong discontinuities of layer interfaces (unless of course κ_h is large, but this can have adverse effects, with the resulting diffusive fluxes forming an unphysical contribution to the volume fluxes used in tracer advection). Some persistent jumps can indeed occur near the topography where the coordinate transition to a quasi-Eulerian system. To limit this, and following Toy and Randall (2008), we added conditional thickness diffusion terms, both in the vertical and horizontal directions. These terms, implemented as lateral second and fourth order diffusion and vertical second order diffusion operators, make use of strong additional diffusivities (e.g., close to what theoretical numerical stability requires), $\kappa_{2h}^{\text{smooth}}$, $\kappa_{4h}^{\text{smooth}}$ and $\kappa_{v}^{\text{smooth}}$. The additional terms read:

$$
\begin{aligned}
\left(\partial_t z^{\sim}\right)_{\text{smoothing}} = & \max\left\{0, \kappa_{2h}^{\text{smooth}}\left[\left|\nabla_h^2 z^{\sim}\right| - \left(\nabla_h^2 z^{\sim}\right)_{\max}\right]\right\} sgn\left(\nabla_h^2 z^{\sim}\right) \\
& -\max\left\{0, \kappa_{4h}^{\text{smooth}}\left[\left|\nabla_h^4 z^{\sim}\right| - \left(\nabla_h^4 z^{\sim}\right)_{\max}\right]\right\} sgn\left(\nabla_h^4 z^{\sim}\right) \\
& +\max\left\{0, \kappa_{v}^{\text{smooth}}\left[\left|\partial_{k,z}^2 z^{\sim}\right| - \left(\partial_{k,z}^2 z^{\sim}\right)_{\max}\right]\right\} sgn\left(\partial_{k,z}^2 z^{\sim}\right)
\end{aligned}
\tag{A8}
$$

where $\left(\nabla_h^2 z^{\sim}\right)_{\max} = 0.01(\Delta x \Delta y)^{-\frac{1}{2}}$, $\left(\nabla_h^4 z^{\sim}\right)_{\max} = 0.01(\Delta x \Delta y)^{-\frac{3}{2}}$, and $\left(\partial_{k,z}^2 z^{\sim}\right)_{\max} = 0.5$ are the specified values chosen here (Δx and Δy being the grid sizes).

A.2.5. Interaction With Barotropic/Baroclinic Mode Splitting

The corrective fluxes arising from the FCT scheme in Equation A7-1 do not guarantee that the vertically integrated transport matches that which comes out of the barotropic loop. This leads to different estimates of the total depth, for example, $\int_{k_b}^{k_t} e_3^{\sim} dk \neq H + \eta$ that should be reconciled. Several strategies exist, such as the iterative one proposed by Hallberg and Adcroft (2009). We have chosen here, for its simplicity, the "upstream" correction of barotropic fluxes as proposed by Higdon (2005); we observe that in the present configuration this scheme does not appear to spin up strong Taylor caps over isolated topography, as was described in the latter paper, and conclude that the restoration to z^* is strong enough to prevent this from occurring.

A.2.6. Additional Comment Concerning Stability

The present Arbitrary Lagrangian-Eulerian implementation is not formulated using an implicit vertical remapping stage, as for instance is the case in Hybrid-Coordinate Ocean Model or version six of the Modular Ocean Model. In these models, once the new vertical grid is known, prognostic variables are remapped in the vertical, while our implementation still relies on the diagnosed cross-layer velocities and the vertical advection step to do so. There are no stability issues associated with the remapping approach, but in the present case the explicit vertical advection stage can seriously limit the permissible time step, especially with large changes in layer interfaces occurring during the regularization step. To mitigate this problem, an unconditionally stable, mixed explicit/implicit vertical advection is used (Shchepetkin, 2015).

Since the present study is not focused on shelves, to prevent possible instabilities developing in shallow water the $z^{\sim}$ coordinate progressively ramps down for depths shallower than 100 m and completely reverts to z^* for $H \leq 50$m.

Appendix B: Code Documentation and Availability

The source code for the modified GO8p0 version of the NEMO v4.0 configuration used in these integrations, along with the namelists and XML files, is archived at Zenodo: https://zenodo.org/record/6652361.

The following preprocessing keys were applied in building GO8p0: key_trabbl; key_si3; key_zdftke; key_zdfddm; key_mpp_mpi; key_mpp_rep; key_nosignedzero; key_iomput.

Data Availability Statement

The derived data used for the analyses and plots are available at https://doi.org/10.5281/zenodo.6076410.

Acknowledgments

This work has been carried out as part of the project "Reducing numerical mixing resulting from applying tides explicitly in a global ocean model" (RENUMERATE) under the Copernicus Marine Environment Monitoring Service (CMEMS). CMEMS is implemented by Mercator Ocean International, in the framework of a delegation agreement with the European Union. It was also co-funded by the Natural Environment Research Council (NERC) under the Climate Linked Atlantic Sector Science (CLASS) marine research program (NE/R015953/1), which supports the Joint Marine Modelling Programme (JMMP), a partnership between the Met Office, National Oceanography Centre, British Antarctic Survey and the Centre for Polar Observation and Modelling. The authors are grateful to the four anonymous reviewers, whose comments and suggestions have significantly improved the paper. The authors would like to thank Mike Bell, Diego Bruciaferri, Pierre Mathiot, Adrian New, and Bablu Sinha for helpful suggestions and advice. The model was integrated on the MONSooN system, a collaborative HPC facility supplied under JMMP, while the analysis was carried out on the JASMIN platform, funded by the NERC and maintained by the Centre for Environmental Data Analysis (CEDA).

References

Adcroft, A., Anderson, W. G., Balaji, V., Blanton, C., Bushuk, M., Dufour, C. O., et al. (2019). The GFDL global ocean and sea ice model OM4.0: Model description and simulation features. *Journal of Advances in Modeling Earth Systems*, *11*(10), 3167–3211. https://doi.org/10.1029/2019MS001726

Adcroft, A., & Campin, J.-M. (2004). Rescaled height coordinates for accurate representation of free-surface flows in ocean circulation models. *Ocean Modelling*, *7*(3–4), 269–284. https://doi.org/10.1016/j.ocemod.2003.09.003

Adcroft, A., & Hallberg, R. (2006). On methods for solving the oceanic equations of motion in generalized vertical coordinates. *Ocean Modelling*, *11*(1–2), 224–233. https://doi.org/10.1016/j.ocemod.2004.12.007

Adcroft, A., Hallberg, R., & Harrison, M. (2008). A finite volume discretization of the pressure gradient force using analytic integration. *Ocean Modelling*, *22*(3–4), 106–113. https://doi.org/10.1016/j.ocemod.2008.02.001

Alford, M. H., Mackinnon, J. A., Simmons, H. L., & Nash, J. D. (2016). Near-inertial internal gravity waves in the ocean. *Annual Review of Marine Science*, *8*(1), 95–123. https://doi.org/10.1146/annurev-marine-010814-015746

Barnier, B., Madec, G., Penduff, T., Molines, J.-M., Treguier, A.-M., Le Sommer, J., et al. (2006). Impact of partial steps and momentum advection schemes in a global ocean circulation model at eddy-permitting resolution. *Ocean Dynamics*, *56*(5–6), 543–567. https://doi.org/10.1007/s10236-006-0082-1

Blaker, A. T., Hirschi, J. J.-M., Bell, M. J., & Bokota, A. (2021). Wind-driven oscillations in the meridional overturning circulation near the equator. Part I: Numerical models. *Journal of Physical Oceanography*, *51*(3), 645–661. https://doi.org/10.1175/JPO-D-19-0296.1

Blaker, A. T., Hirschi, J. J.-M., Sinha, B., de Cuevas, B., Alderson, S., Coward, A., & Madec, G. (2012). Large near-inertial oscillations of the Atlantic meridional overturning circulation. *Ocean Modelling*, *42*, 50–56. https://doi.org/10.1016/j.ocemod.2011.11.008

Bleck, R. (2002). An oceanic general circulation model framed in hybrid isopycnic-cartesian coordinates. *Ocean Modelling B*, *4*(1), 55–88. https://doi.org/10.1016/s1463-5003(01)00012-9

Bleck, R., & Smith, L. T. (1990). A wind-driven isopycnic coordinate model of the North and Equatorial Atlantic Ocean. 1: Model development and supporting experiments. *Journal of Geophysical Research*, *95*(C3), 3273–3285. https://doi.org/10.1029/jc095ic03p03273

Bruciaferri, D., Shapiro, G. I., & Wobus, F. (2018). A multi-envelope vertical coordinate system for numerical ocean modelling. *Ocean Dynamics*, *68*(10), 1239–1258. https://doi.org/10.1007/s10236-018-1189-x

Bryan, K., Manabe, S., & Pacanowski, R. C. (1975). A global ocean atmosphere climate model. Part II. The oceanic circulation. *Journal of Physical Oceanography*, *5*(1), 30–46. https://doi.org/10.1175/1520-0485(1975)005<0030:agoacm>2.0.co;2

Colombo, P., Barnier, B., Penduff, T., Chanut, J., Deshayes, J., Molines, J.-M., et al. (2020). Representation of the Denmark Strait overflow in a *z*-coordinate eddying configuration of the NEMO (v3.6) Ocean model: Resolution and parameter impacts. *Geoscientific Model Development*, *13*(7), 3347–3371. https://doi.org/10.5194/gmd-13-3347-2020

Cox, M. D. (1987). Isopycnal diffusion in a *z*-coordinate ocean model. *Ocean Modelling*, *74*, 1–5.

Dickson, B., Meincke, J., & Rhines, P. (2008). Arctic–subarctic ocean fluxes: Defining the role of the northern seas in climate. In R. R. Dickson, J. Meincke, & P. Rhines (Eds.), *Arctic–Subarctic ocean fluxes*. Springer. https://doi.org/10.1007/978-1-4020-6774-7_1

Dunne, J. P., John, J., Adcroft, A., Griffies, S. M., Hallberg, R. W., Shevliakova, E., et al. (2012). GFDL's ESM2 global coupled climate-carbon Earth System Models Part I: Physical formulation and baseline simulation characteristics. *Journal of Climate*, *25*(19), 6646–6665. https://doi.org/10.1175/JCLI-D-11-00560.1

Emery, W. J., & Meincke, J. (1986). Global water masses: Summary and review. *Oceanologica Acta*, *9*, 383–391.

Gargett, A. E., & Holloway, G. (1984). Dissipation and diffusion by internal wave breaking. *Journal of Marine Research*, *42*(1), 15–27. https://doi.org/10.1357/002224084788506158

Gaspar, P., Grégoris, Y., & Lefevre, J.-M. (1990). A simple eddy kinetic energy model for simulations of the oceanic vertical mixing: Tests at station Papa and Long-Term Upper Ocean Study Site. *Journal of Geophysical Research*, *95*(C9), 16179–16193. https://doi.org/10.1029/JC095iC09p16179

Gibson, A. H., Hogg, A. M., Kiss, A. E., Shakespeare, C. J., & Adcroft, A. (2017). Attribution of horizontal and vertical contributions to spurious mixing in an Arbitrary Lagrangian-Eulerian ocean model. *Ocean Modelling*, *119*, 45–56. https://doi.org/10.1016/j.ocemod.1564.2017.09.008

Good, S. A., Martin, M. J., & Rayner, N. A. (2013). EN4: Quality controlled ocean temperature and salinity profiles and monthly objective analyses with uncertainty estimates. *Journal of Geophysical Research: Oceans*, *118*(12), 6704–6716. https://doi.org/10.1002/2013jc009067

Griffies, S. M., Adcroft, A., & Hallberg, R. (2020). A primer on the vertical Lagrangian-remap method in ocean models based on finite volume generalized vertical coordinates. *Journal of Advances in Modeling Earth Systems*, *12*(10), e2019MS001954. https://doi.org/10.1029/2019MS001954

Griffies, S. M., Gnanadesikan, A., Pacanowski, R. C., Larichev, V. D., Dukowicz, J. K., & Smith, R. D. (1998). Isoneutral diffusion in a *z*-coordinate ocean model. *Journal of Physical Oceanography*, *28*(5), 805–830. https://doi.org/10.1175/1520-0485(1998)028<0805:idiazc>2.0.co;2

Griffies, S. M., & Hallberg, W. R. (2000). Biharmonic friction with a Smagorinsky-like viscosity for use in large-scale eddy-permitting ocean models. *Monthly Weather Review*, *128*(8), 2935–2946. https://doi.org/10.1175/1520-0493(2000)128<2935:bfwasl>2.0.co;2

Griffies, S. M., Pacanowski, R. C., & Hallberg, R. W. (2000). Spurious diapycnal mixing associated with advection in a *z*-coordinate ocean model. *Monthly Weather Review*, *128*(3), 538–564. https://doi.org/10.1175/1520-0493(2000)128<0538:sdmawa>2.0.co;2

Hallberg, R. (2013). Using a resolution function to regulate parameterizations of oceanic mesoscale eddy effects. *Ocean Modelling*, *72*, 92–103. https://doi.org/10.1016/j.ocemod.2013.08.007

Hallberg, R., & Adcroft, A. (2009). Reconciling estimates of the free surface height in Lagrangian vertical coordinate ocean models with mode-split time stepping. *Ocean Modelling*, *29*(1), 15–26. https://doi.org/10.1016/j.ocemod.2009.02.008

Higdon, R. L. (2005). A two-level time-stepping method for layered ocean circulation models: Further development and testing. *Journal of Computational Physics*, *206*(2), 463–504. https://doi.org/10.1016/j.jcp.2004.12.011

Hirschi, J. J.-M., Barnier, B., Böning, C., Biastoch, A., Blaker, A. T., Coward, A., et al. (2020). The Atlantic meridional overturning circulation in high resolution models. *Journal of Geophysical Research: Oceans*, *125*(4), e2019JC015522. https://doi.org/10.1029/2019JC015522

Holmes, R. M., Zika, J. D., Griffies, S. M., Hogg, A. M., Kiss, A. E., & England, M. H. (2021). The geography of numerical mixing in a suite of global ocean models. *Journal of Advances in Modeling Earth Systems*, *13*(7), e2020MS002333. https://doi.org/10.1029/2020MS002333

Ilıcak, M. (2016). Quantifying spatial distribution of spurious mixing in ocean models. *Ocean Modelling*, *108*, 30–38. https://doi.org/10.1016/j.ocemod.2016.11.002

Ilıcak, M., Adcroft, A. J., Griffies, S. M., & Hallberg, R. W. (2012). Spurious dianeutral mixing and the role of momentum closure. *Ocean Modelling*, *45–46*, 37–58. https://doi.org/10.1016/j.ocemod.2011.10.003

Jackson, L. C., Dubois, C., Forget, G., Haines, K., Harrison, M., Iovino, D., et al. (2019). The mean state and variability of the north Atlantic circulation: A perspective from ocean reanalyses. *Journal of Geophysical Research: Oceans*, *124*(12), 9141–9170. https://doi.org/10.1029/2019JC015210

Klocker, A., & McDougall, T. J. (2010). Influence of the nonlinear equation of state on global estimates of dianeutral advection and diffusion. *Journal of Physical Oceanography*, *40*(8), 1690–1709. https://doi.org/10.1175/2010jpo4303.1

Large, W., & Yeager, S. (2009). The global climatology of an interannually varying air–sea flux data set. *Climate Dynamics*, *33*(2–3), 341–364. https://doi.org/10.1007/s00382-008-0441-3

Leclair, M., & Madec, G. (2009). A conservative leapfrog time stepping method. *Ocean Modelling*, *30*(2–3), 88–94. https://doi.org/10.1016/j.ocemod.2009.06.006

Leclair, M., & Madec, G. (2011). $z\tilde{}$-Coordinate, an Arbitrary Lagrangian–Eulerian coordinate separating high and low frequency motions. *Ocean Modelling*, *37*(3–4), 139–152. https://doi.org/10.1016/j.ocemod.2011.02.001

Lee, M.-M., Coward, A. C., & Nurser, A. G. (2002). Spurious diapycnal mixing of deep waters in an eddy-permitting global ocean model. *Journal of Physical Oceanography*, *32*(5), 1522–1535. https://doi.org/10.1175/1520-0485(2002)032<1522:sdmotd>2.0.co;2

Levier, B., Tréguier, A.-M., Madec, G., & Garnier, V. (2007). Free surface and variable volume in the NEMO code (Tech. Rep., MERSEA IP report WP09-CNRS-STR-03-1A, p. 47). Retrieved from https://zenodo.org/record/3244182/export/hx#.Y1JaqS8w1R4

Madec, G., Bourdallé-Badie, R., Chanut, J., Clementi, E., Coward, A., Ethé, C., et al. (2019). NEMO ocean engine. *Notes du Pole de Modélisation de l'Institut Pierre-Simon Laplace (IPSL)*, *27*, 386. https://doi.org/10.5281/zenodo.3878122

Marzocchi, A., Hirschi, J. J.-M., Holliday, N. P., Cunningham, S. A., Blaker, A. T., & Coward, A. C. (2015). The North Atlantic subpolar circulation in an eddy-resolving global ocean model. *Journal of Marine Systems*, *142*, 126–143. https://doi.org/10.1016/j.jmarsys.2014.10.007

McDonagh, E. L., McLeod, P., King, B. A., Bryden, H. L., & Valdes, S. T. (2010). Circulation, heat, and freshwater transport at 36 N in the Atlantic. *Journal of Physical Oceanography*, *40*(12), 2661–2678. https://doi.org/10.1175/2010JPO4176.1

Megann, A. (2018). Estimating the numerical diapycnal mixing in an eddy-permitting ocean model. *Ocean Modelling*, *121*, 19–33. https://doi.org/10.1016/j.ocemod.2017.11.001

Megann, A., Blaker, A., Josey, S., New, A., & Sinha, B. (2021). Mechanisms for late 20th and early 21st century decadal AMOC variability. *Journal of Geophysical Research: Oceans*, *126*(12). https://doi.org/10.1029/2021JC017865

Megann, A., & Storkey, D. (2021). Exploring viscosity space in an eddy-permitting global ocean model: Is viscosity a useful control for numerical mixing? *Journal of Advances in Modeling Earth Systems*, *13*(5), e2020MS002263. https://doi.org/10.1029/2020MS002263

Megann, A. P., New, A. L., Blaker, A. T., & Sinha, B. (2010). The sensitivity of a coupled climate model to its ocean component. *Journal of Climate*, *23*(19), 5126–5150. https://doi.org/10.1175/2010JCLI3394.1

Petersen, M. R., Jacobsen, D. W., Ringler, T. D., Hecht, M. W., & Maltrud, M. E. (2015). Evaluation of the Arbitrary Lagrangian–Eulerian vertical coordinate method in the MPAS-ocean model. *Ocean Modelling*, *86*, 93–113. https://doi.org/10.1016/j.ocemod.2014.12.004

Redi, M. H. (1982). Oceanic isopycnal mixing by coordinate rotation. *Journal of Physical Oceanography*, *12*(10), 1154–1158. https://doi.org/10.1175/1520-0485(1982)012<1154:oimbcr>2.0.co;2

Rousset, C., Vancoppenolle, M., Madec, G., Fichefet, T., Flavoni, S., Barthélemy, A., et al. (2015). The Louvain-La-Neuve Sea Ice model LIM3.6: Global and regional capabilities. *Geoscientific Model Development*, *8*(10), 2991–3005. https://doi.org/10.5194/gmd-8-2991-2015

Sellar, A. A., Jones, C. G., Mulcahy, J., Tang, Y., Yool, A., Wiltshire, A., et al. (2019). UKESM1: Description and evaluation of the UK Earth system model. *Journal of Advances in Modeling Earth Systems*, *11*(12), 4513–4558. https://doi.org/10.1029/2019MS001739

Shchepetkin, A. F. (2015). An adaptive, Courant-number-dependent implicit scheme for vertical advection in oceanic modeling. *Ocean Modelling*, *91*, 38–69. https://doi.org/10.1016/j.ocemod.2015.03.006

Shchepetkin, A. F., & McWilliams, J. C. (2003). A method for computing horizontal pressure-gradient force in an oceanic model with a nonaligned vertical coordinate. *Journal of Geophysical Research*, *108*(C3), 1–34. https://doi.org/10.1029/2001jc001047

Simmons, H. L., Jayne, S. R., St. Laurent, L. C., & Weaver, A. J. (2004). Tidally driven mixing in a numerical model of the ocean general circulation. *Ocean Modelling*, *6*(3–4), 245–263. https://doi.org/10.1016/s1463-5003(03)00011-8

Smeed, D. A., Josey, S. A., Beaulieu, C., Johns, W. E., Moat, B. I., Frajka-Williams, E., et al. (2018). The North Atlantic Ocean is in a state of reduced overturning. *Geophysical Research Letters*, *45*(3), 1527–1533. https://doi.org/10.1002/2017GL076350

Stacey, M. W., Pond, S., & Nowak, Z. P. (1995). A numerical model of the circulation in Knight Inlet, British Columbia, Canada. *Journal of Physical Oceanography*, *25*(6), 1037–1062. https://doi.org/10.1175/1520-0485(1995)025<1037:anmotc>2.0.co;2

Storkey, D., Blaker, A. T., Mathiot, P., Megann, A., Aksenov, Y., Blockley, E. W., et al. (2018). UK global ocean GO6 and GO7: A traceable hierarchy of model resolutions. *Geoscientific Model Development*, *11*(8), 3187–3213. https://doi.org/10.5194/gmd-11-3187-2018

Toy, M. D., & Randall, D. A. (2008). Design of a Nonhydrostatic atmospheric model based on a generalized vertical coordinate. *Monthly Weather Review*, *137*(7), 2305–2330. https://doi.org/10.1175/2009mwr2834.1

Urakawa, S., & Hasumi, H. (2014). Effect of numerical diffusion on the water mass transformation in eddy-resolving models. *Ocean Modelling*, *74*, 22–35. https://doi.org/10.1016/j.ocemod.2013.11.003

Walin, G. (1982). On the relation between sea-surface heat flow and thermal circulation in the ocean. *Tellus*, *34*(2), 187–195. https://doi.org/10.1111/j.2153-3490.1982.tb01806.x

Williams, K. D., Copsey, D., Blockley, E. W., Bodas-Salcedo, A., Calvert, D., Comer, R., et al. (2018). The Met Office global coupled model 3.0 and 3.1 (GC3.0 & GC3.1) configurations. *Journal of Advances in Modeling Earth Systems*, *9*(2), 357–380. https://doi.org/10.1002/2017MS001115

Winton, M., Hallberg, R., & Gnanadesikan, A. (1998). Simulation of density-driven frictional downslope flow in z-coordinate ocean models. *Journal of Physical Oceanography*, *68*(11), 2163–2174. https://doi.org/10.1175/1520-0485(1998)028<2163:soddfd>2.0.co;2

Wise, A., Harle, J., Bruciaferri, D., O'Dea, E., & Polton, J. (2022). The effect of vertical coordinates on the accuracy of a shelf sea model. *Ocean Modelling*, *170*, 101935. https://doi.org/10.1016/j.ocemod.2021.101935

Worthington, L. V. (1981). The water masses of the world ocean: Some results of a fine-scale census. In B. A. Warren & C. Wunsch (Eds.), *Evolution of physical oceanography* (Chap. 2, pp. 42–69). MIT Press.

Wunsch, C. (1975). Internal tides in the ocean. *Reviews of Geophysics*, *13*(1), p167–p182. https://doi.org/10.1029/RG013i001p00167

Zalesak, S. T. (1979). Fully multidimensional flux corrected transport algorithms for fluids. *Journal of Computational Physics*, *31*(3), 335–362. https://doi.org/10.1016/0021-9991(79)90051-2